ARMY RESEARCH LABORATORY

Description of the Battlescale Forecast Model

By Teizi Henmi
Robert Dumais, Jr.

Information Science and Technology Directorate
Battlefield Environment Division

ARL-TR-1032 May 1998

NOTICES

Disclaimers

The findings in this report are not to be construed as an official Department of the Army position unless so designated by other authorized documents.

The citation of trade names and names of manufacturers in this report is not to be construed as official Government indorsement or approval of commercial products or services referenced herein.

REPORT DOCUMENTATION PAGE

Form Approved
OMB No. 0704-0188

1. AGENCY USE ONLY (Leave Blank)	2. REPORT DATE	3. REPORT TYPE AND DATES COVERED
	May 1998	Final

4. TITLE AND SUBTITLE
Description of the Battlescale Forecast Model

5. FUNDING NUMBERS

6. AUTHOR(S)
Teizi Henmi and Robert Dumais, Jr.

7. PERFORMING ORGANIZATION NAME(S) AND ADDRESS(ES)
U.S. Army Research Laboratory
Battlefield Environment Directorate
Attn: AMSEL-IS-W
White Sands Missile Range, NM 88002-5501

8. PERFORMING ORGANIZATION REPORT NUMBER
ARL-TR-1032

9. SPONSORING/MONITORING AGENCY NAME(S) AND ADDRESS(ES)
U.S. Army Research Laboratory
2800 Powder Mill Road
Adelphi, MD 20783-1145

10. SPONSORING/MONITORING AGENCY REPORT NUMBER
ARL-TR-1032

11. SUPPLEMENTARY NOTES

12a. DISTRIBUTION/AVAILABILITY STATEMENT
Approved for public release; distribution unlimited.

12b. DISTRIBUTION CODE
A

13. ABSTRACT (Maximum 200 words)

The Battlescale Forecast Model, which was developed at the U.S. Army Research Laboratory, is a major part of the U.S. Army Integrated Meteorological System Block II software. The Battlescale Forecast Model can be used operationally over any part of the world by using meteorological data obtained through the Automated Weather Distribution System. The Integrated Weather Effects Decision Aids utilize the Battlescale Forecast Model output file to calculate the values of their parameters. The Atmospheric Sounding Program generates products such as probability of thunderstorm occurrence, icing, visibility, and turbulence.

This report describes the theoretical and mathematical principles used in the Battlescale Forecast Model, and shows some examples of input/output data.

14. SUBJECT TERMS
forecast, mesoscale

15. NUMBER OF PAGES
148

16. PRICE CODE

17. SECURITY CLASSIFICATION OF THIS REPORT	18. SECURITY CLASSIFICATION OF THIS PAGE	19. SECURITY CLASSIFICATION OF ABSTRACT	20. LIMITATION OF ABSTRACT
UNCLASSIFIED	UNCLASSIFIED	UNCLASSIFIED	SAR

NSN 7540-01-280-5500

Standard Form 298 (Rev. 2-89)
prescribed by ANSI Std. Z39-18-298-102

Preface

The Battlescale Forecast Model, developed at the U.S. Army Research Laboratory, is a major part of the U.S. Army Integrated Meteorological System Block II software. The Battlescale Forecast Model can be used operationally world-wide by using meteorological data obtained through the Automated Weather Distribution System. The Integrated Weather Effects Decision Aids utilizes the Battlescale Forecast Model output file to calculate the values of their parameters. The Atmospheric Sounding Program generates products such as probability of thunderstorm occurrence, icing, visibility, and turbulence.

This report describes the theoretical and mathematical principles used in the Battlescale Forecast Model, and shows some examples of input/output data.

Contents

Preface 1

Executive Summary 7

1. Introduction 9

2. Terrain Elevation Data File Production 11

3. Three-Dimensional Analysis of Input Data 17

3.1 GSM Data 19

3.2 Upper Air Sounding Data 29

3.3 Compositing the GSM and Upper Air Sounding Data 32

4. Forecast Model 35

4.1 Governing Equations 36

4.2 Surface Boundary Conditions 44

4.3 Surface Energy Balance and Surface Temperature 47

4.4 Radiational Energy Fluxes 52

4.5 Upper Boundary Conditions 57

4.6 Lateral Boundary Conditions 57

4.7 Diagnostic Pressure Distribution 58

4.8 Radiative Effects in Clouds 60

4.8.1 Shortwave Radiation 61

4.8.2 Longwave Radiation 64

4.9 Cloud Condensation 65

4.10 Non-Convective Precipitation Rate 73

4.11 Sea Surface Temperature and Soil Characteristics 76

4.11.1 Sea Surface Temperature 76
4.11.2 Surface Characteristics 76

5. Initialization and Assimilation of Data 77
5.1 Initialization 77
5.2 Nudging Method 78
5.3 Target Winds 80
5.4 Surface Data Nudging 82

6. Initialization Data and Some Examples of the BFM 85
6.1 Qualities of the GSM Forecast Data 86
6.2 Initialization Fields for the BFM Forecasting Calculation 95
6.3 The Effects of the Initial Data Fields on BFM Output at the Surface 101
6.4 Examples of Fog/Low Level Cloud and Non-Convective Precipitation 109

7. Conclusion 115

References 119

Acronyms and Abbreviations 125

Appendix: *List of Symbols* 127

Distribution 137

Figures

1. Schematic diagram showing how the latitude and longitude of model grid points are calculated 13
2. Schematic diagram showing how the elevation values are obtained from the DTED CD-ROM Level 1 data 14
3. Terrain elevation data produced over southern California, centered at the National Training Center, Fort Irwin, CA. 15
4. Distribution of input data over the BFM domain. 18
5. Model vertical level distribution over complex terrain. 22
6. Schematic diagram showing the relationships between the BFM grid points and GSM data points 26
7. Relationships showing R, $Q_l/2\sigma_s$, and $q_c^2/4\sigma_s^2$ as a function of Q_l (= a $(Q_W-Q_{sl})/2\sigma_s$) 72

8A. Relationship between the GSM (top) for the 12-h forecasting data and upper air sounding data for temperature for the 24-h forecast data (bottom) 90

8B. Same as figure 8A, except for dew point temperature 91

8C. Same as figure 8A, except for east-west components of horizontal wind vectors 92

8D. Same as figure 8A, except for north-south components of horizontal wind vectors 93

9. Horizontal wind vector distribution at 10 m AGL, produced by compositing the GSM and upper air sounding data for 12 GMT, 24 Aug 95, over Bosnia 97
10. Surface wind vectors observed at 12 GMT, 24 Aug 96, over Bosnia 97
11. Streamlines and isotachs at the 10-m level, at time $T_0 = 0$ h for surface wind data nudged (top), and for surface wind data not nudged (bottom) .. 98
12. Temperature distribution at the 10-m level, at $T_0 = 0$ h for surface data nudged (top), and for not nudged (bottom) 99

13. Dew point temperature distribution at the 10-m level at $T_0 = 0$ h (top) for surface wind data nudged, and for not nudged (bottom) 100
14. Same as figure 11, except for $T_0 = 3$ h 103
15. Same as figure 11, except for $T_0 = 6$ h 104
16. Same as figure 12, except for $T_0 = 3$ h 105
17. Same as figure 12, except for $T_0 = 6$ h 106
18. Same as figure 13, except for $T_0 = 3$ h 107
19. Same as figure 13, except for $T_0 = 6$ h 108
20. Cloud cover over Bosnia, (top) at 23 GMT on 19 Dec 95, and at 00 GMT on 20 Dec 95 (bottom) 111
21. Vertical profiles of total water content (g/kg), cloud water content (g/kg), and relative humidity (%), at the center of model domain (top) at 00 GMT, and (bottom) at 01 GMT, 20 Dec 95 112
22. Precipitation rate (mm/h) distribution over Bosnia, at 01 GMT, 20 Dec 95. Maximum rate is 1.4 mm/h, and minimum rate is .1 mm/h 113

Tables

1. Z* heights for vertical levels of BFM 21
2. Locations, dates, and hours of upper air sounding data used for comparison with GSM data 87
3. Correlation coefficients between the GSM data and upper air data 89

Executive Summary

Introduction

The U.S. Army Research Laboratory (ARL), Battlefield Environment Directorate (BED) has developed the Battlescale Forecast Model (BFM) for operation of short-range (up to 24-h) forecasting over areas extending up to 500 x 500 km. The BFM is designed so it can be applied world-wide as long as meteorological data is available. Depending on the availability of the input data from the U.S. Air Force Global Spectral Model (GSM), upper air sounding data, and surface data, different combinations of input data are used to initialize the BFM.

Purpose

This report describes the theoretical and mathematical principles used in the BFM. The GSM forecast data, which composes a major part of the input data to the BFM, is compared with observed upper air sounding data. The influences on the BFM forecast field of surface observation data assimilation are also examined. Finally, the capability to forecast stratiform clouds and non-convective precipitation by the BFM are demonstrated.

Overview

For all input data available, the BFM is initialized by the composite data fields from the GSM and upper air sounding data, plus surface meteorological data. For a minimal requirement , the BFM can be initialized by a single sounding profile within the model domain and produce forecast field for 6 h.

The BFM is composed of elements such as:

- a terrain elevation data production program;
- three dimensional data analysis program for model initialization and data assimilation;
- a prognostic mesoscale model, the Higher Order Turbulence Model for Atmospheric Circulation (HOTMAC);
- horizontal and vertical displays of its outputs;
- input/output data archiving system; and
- a map background module to help visualize both execution and display.

1. Introduction

The U.S. Army Research Laboratory, Battlefield Environment Directorate (ARL, BED) has developed the Battlescale Forecast Model (BFM) for short-range weather forecasting over areas of 500 x 500 km or smaller. The BFM can also be used world-wide by using meteorological data obtained through the Automated Weather Distribution System (AWDS). It is a major part of the U.S. Army Integrated Meteorological System (IMETS) Block II software. Meteorological data includes the U.S. Air Force Global Spectral Model (GSM) grided forecast data, in addition to conventional upper air sounding and surface data.

The BFM is composed of:

- A terrain elevation data production program;
- Three-dimensional data analysis programs of input data for model initialization and data assimilation;
- A prognostic mesoscale model, called the Higher Order Turbulence Model of Atmospheric Circulation (HOTMAC); and
- Model output interpolation programs to display horizontally (at desired heights) and vertically (at model levels) for any desired grid location.

The BFM has been used successfully in exercises such as the Department of Defense's Operation Desert Capture II and the NATO's Atlantic Resolve 1994. Since December 1995 it has been employed at Heidelberg, Germany, by the 617th Weather Squadron to forecast weather over Bosnia.

The objectives of this report are to describe the theoretical and mathematical principles used in the BFM (mainly elements one through three), and to show some examples of input/output data.

This report describes the method of obtaining digital terrain elevation data and the methods of three-dimensional data analysis of meteorological data. The prognostic mesoscale forecast model, HOTMAC, is summarized from the original developer's publications. The report also describes the methods of initialization and data assimilation. Examples of the BFM input/output are given to show the capabilities of the model.

2. Terrain Elevation Data File Production

The elevation data file for BFM execution is produced by reading the Digital Terrain Elevation Data (DTED) CDROMs from the Defense Mapping Agency (DMA). DTED is a uniform matrix of digital terrain elevation values. Each matrix point represents geographic coordinates with a corresponding elevation value above mean sea level (MSL). Level 1 DTED (DTED1) matrix point spacing is 3 arc s or approximately 100 m. [1]

The horizontal grid spacings of the BFM are linear, and the maximum integration domain has a horizontal extent of 500 km, although the input data collection area can have a horizontal extent as large as 1600 km. At such distances, it is a good assumption that the earth is a perfect sphere when determining the latitudes and longitudes of individual grid points. However, for horizontal extents beyond about 1000 km, this assumption loses some validity. Still, the errors introduced should be relatively small.

First, we calculate the latitudes and longitudes of the BFM grid points by using the following equations. Figure 1 shows that the latitude and longitude of a grid point (i, j) is calculated as:

$$GLON(i,j)=LON_0+\frac{\Delta\cdot(i-\frac{(i_{\max}+1)}{2})}{R_E\cdot(\frac{\pi}{180})\cdot\cos[\frac{\pi}{180}\cdot GLAT(j)]} \qquad (1)$$

$$GLAT(j) = LAT_0 + \frac{\Delta \cdot \left(j - \frac{(j_{max}+1)}{2}\right)}{R_E \cdot \left(\frac{\pi}{180}\right)} \qquad (2)$$

where

R_E = the radius of the earth

Δ = the unit grid space

LON_0 = longitude of the center of the model domain,

LAT_0 = latitude of the center of the model domain,

and

(i_{max}, j_{max}) = the maximum numbers of grid points for the (x,y) directions,

where

(i, j) = the grid point counters in x- and y- directions.

The values of i_{max} and j_{max} are fixed in the model to values of 161 x 161. This means that for a horizontal spacing of 10 km, terrain data must be generated for an area of 1600 x 1600 km for the three-dimensional analysis to be executed. The southwest corner of the domain is represented by (1, 1), and the northeast corner is represented by (i_{max}, j_{max}).

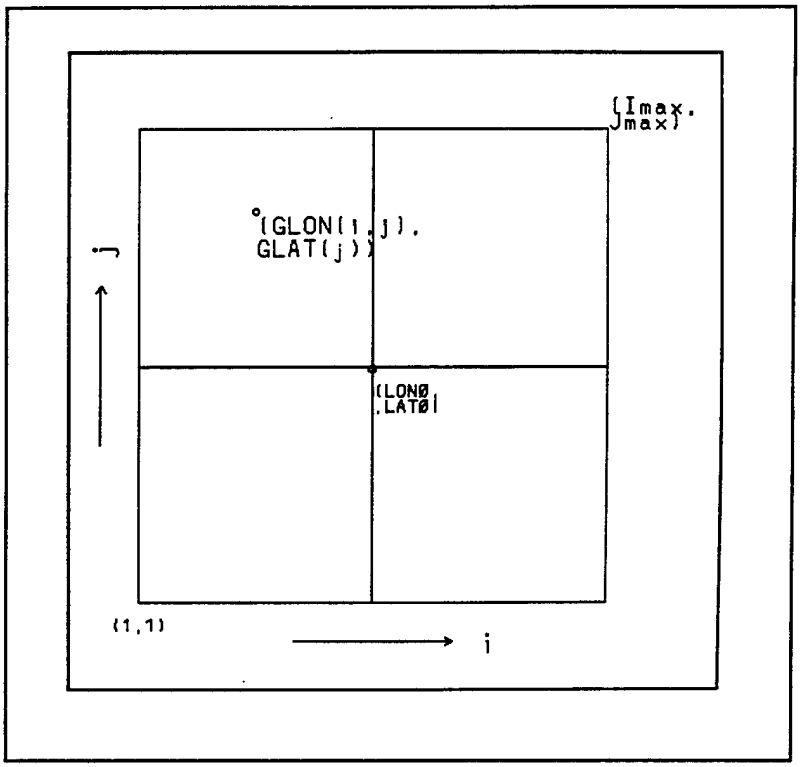

Figure 1. Schematic diagram showing how the latitude and longitude of model grid points are calculated.

Next, the terrain height at (i, j), GZ (i, j), is interpolated from the data of the four surrounding matrix points that are read from the DTED CDROM. Referring to figure 2 let's define:

$$t=\frac{GLON(i,j)-LON_w}{LON_e-LON_w} \tag{3}$$

$$u=\frac{GLAT(i)-LAT_s}{LAT_n-LAT_s} \tag{4}$$

Here,

t = the dimensionless longitudinal distance to (i, j) from the western longitude of the DTED data that surround the grid point (i, j).

Similarly,

u = the dimensionless latitudinal distance to (i, j) from the southern latitude of surrounding DTED data.

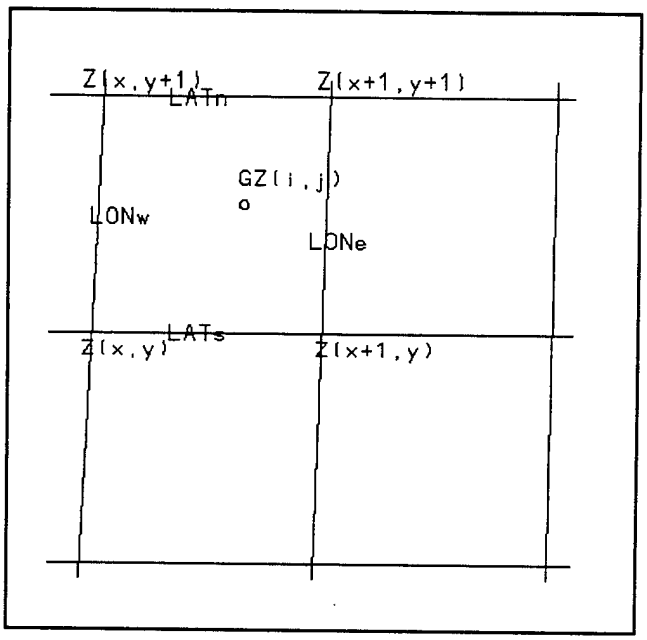

Figure 2. Schematic diagram showing how the elevation values are obtained from the DTED CD-ROM Level 1 data.

The terrain elevation at the grid point (i, j) is determined by

$$GZ(i,j) = (1-t)\cdot(1-u)\cdot Z(x,y) + t\cdot(1-u)\cdot Z(x+1,y) + (1-t)\cdot u\cdot Z(x,y+1) + t\cdot u\cdot Z(x+1,y+1) \quad (5)$$

where

GZ = terrain elevation of the BFM grid point,

Z = a DTED elevation data point.

The above process is repeated for every grid point of the BFM.

Figure 3 is an example of elevation data obtained for the southwestern United States centered at the National Training Center, Fort Irwin, CA. Data is produced for the area of 1,600 x 1,600 km with unit grid spacing of 10 km. The internal square area is the BFM domain, covering 500 x 500 km. Both grid squares share the same center coordinates.

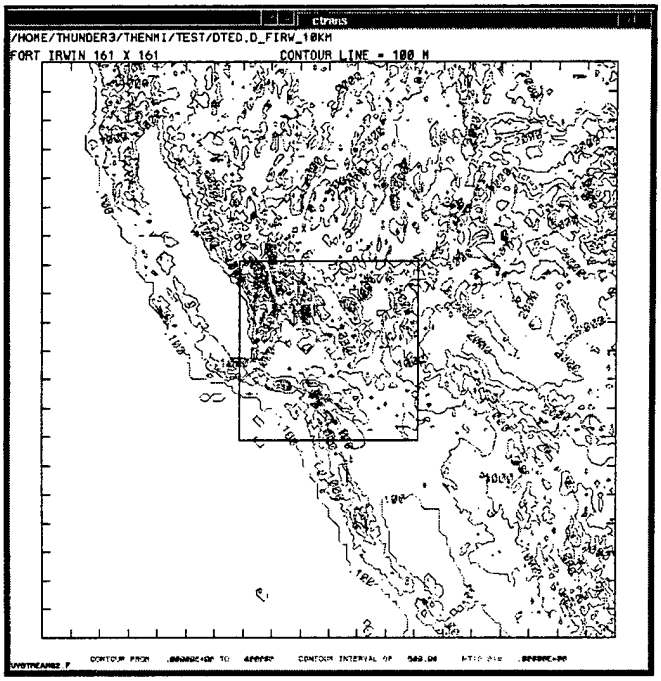

Figure 3. Terrain elevation data produced over southern California, centered at the National Training Center, Fort Irwin, CA.

3. Three-Dimensional Analysis of Input Data

The BFM forecast calculations are made by using the GSM grided forecast fields, upper air radiosonde observations, and surface sensor observations as initial input and time-dependent lateral boundary condition data. This data is regularly communicated to the IMETS workstation computer through the AWDS from the Air Force Global Weather Center (AFGWC), or manually input. Objectively analyzed three-dimensional data fields for model initialization can be provided by three different data sources:

- GSM data,
- Upper air data, and
- Combination of GSM and upper air data.

Each of the above can be considered a separate analysis "mode." Depending on the availability and the quality of data, any of the above modes can be selected for initialization analysis. Surface sensor data is not used to make three-dimensional data fields; it is used to initialize the BFM prognostic calculations in a different way.

Figure 4 shows the distribution of the different input data. "G" represents the GSM data locations, "U" the upper air radiosondes, and "S" the surface data sites. The center of the model domain was chosen to be at 18.657 E and 44.470 N. The entire domain covers a 1600 x 1600 km area (161 x 161 grid points with a unit grid distance of 10 km), and the inner square covers a sub-area of 500 x 500 km (51 x 51 grid points). The large square covers a 1,600 x 1,600 km area. The inner square of the BFM domain covers a 500 x 500 km area. The area is centered at Tuzla, Bosnia, located at 44.470 N and 18.657 E. "G" is located at the GSM data points, "U" at the upper air sounding sites, and "S" at the surface observation sites.

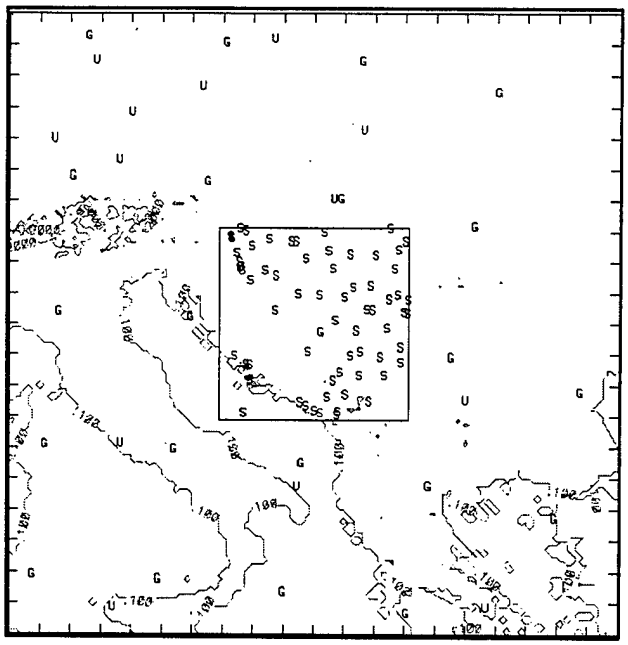

Figure 4. Distribution of input data over the BFM domain.

The GSM data and/or upper air radiosonde data available in the large square is used to produce objectively analyzed three-dimensional meteorological data fields at the horizontal resolution required by the model. Then, the data fields within the inner square sub-region are used to initialize the BFM forecast model.

In all the above three methods, the analysis was performed over a large domain of 161 x 161 grid by using z^* defined by equation (6), in which z_{gmax2} is the maximum height in the 161 x 161 grid domain. A forecast calculation is typically done over a 51 x 51 grid domain located at the central part of the large domain where the maximum height is z_{gmax}. In the case where z_{gmax} is smaller than z_{gmax2}, all the parameters are adjusted linearly to the new z^* levels defined by replacing z_{gmax2} by z_{gmax}. The three-dimensional fields covering the 51 x 51 x 16 subgrid are used to initialize the BFM.

3.1 GSM Data

The GSM forecast calculations are made regularly at the base times of 00 and 12 Greenwich Meridian Time (GMT). Forecast results become available to the IMETS approximately 7 h after the base times. For instance, if the BFM forecast calculation is made at a base time between 00 and 12 GMT, the GSM forecast data based at 00 GMT is not available until about 07 GMT; the calculations are based at 12 GMT of the previous day are available. To avoid the data-absent period, the 12, 24, 36, and 48-h forecast data generated at the base time of 12 GMT of the previous day are used. When the BFM forecast base time is between the 12 and 24-h GSM forecast time, the initial BFM field is constructed by linearly interpolating between the 12 and 24-h GSM forecast fields (in addition to combining and compositing available upper air radiosonde data). Similarly, the GSM derived forecast fields used by the BFM as time dependent lateral boundary values (out to 24 h), can be obtained by linear interpolations of the appropriate GSM fields: 24, 36, and 48 h.

Due to current design constraints, although a new GSM base time forecast arrives to the IMETS about 7 h later, this data is not accessed until exactly 12 h after the new base time. Therefore, for a BFM initialization 11 h after either the 12 GMT or 00 GMT GSM base times (23 GMT or 11 GMT, respectively), GSM 23-h forecast data is used to generate the BFM initialization fields (along with available upper air and surface data). Additionally, GSM 47-h forecast data would be used as the BFM 24-h lateral boundary condition data. A new design is being considered that would make the new GSM base time forecasts available to the BFM immediately upon arrival to the IMETS.

The following GSM products on the whole-mesh grid (unit grid space is 381 km at 60° N or S and a function of latitude [2]) on six constant pressure levels (200, 300, 500, 700, 850, and 1000 mb) are used:

ϕ = Geopotential height,

T = Temperature,

$(T - T_d)$ = Dew point depression,

(U, V) = Horizontal wind vector components.

A fictitious 1070 mb level is created, with data extrapolated down from the 1000 mb level to ensure that data exists down to the minimum terrain elevation of the 161 x 161 grid. Using the above parameters, three-dimensional fields on (x, y, z*) coordinates of the following parameters are produced:

Θ_v = Virtual potential temperature (K),

Q_v = Water vapor mixing ratio (g/kg),

U = East-west component of wind,

V = North-south component of wind,

P_{gr} = Surface pressure distribution,

where

z* = vertical coordinate used in HOTMAC, and defined as:

$$z^* = \overline{H}\frac{z - z_g}{H - z_g} \qquad (6)$$

where

z = the Cartesian vertical coordinate,

z_g = the ground elevation,

H = the material surface top of the model in the z^* coordinate,

and

H = the corresponding height in the z coordinate defined by $H=\overline{H} + z_{gmax}$

where

z_{gmax} = the maximum value of the terrain elevation in the BFM domain.

Currently, the vertical extent of the model is 7000 m above the highest grid point of the BFM domain. Table 1 show the variables as calculated at the following 16 vertical levels:

Table 1. Z* heights for vertical levels of BFM

Level	z* height (m)
1	0.0
2	2.0
3	6.0
4	10.0
5	14.0
6	32.3
7	151.0
8	384.5
9	732.6
10	1195.4
11	1773.0
12	2465.3
13	3272.2
14	4193.9
15	5230.3
16	6381.4

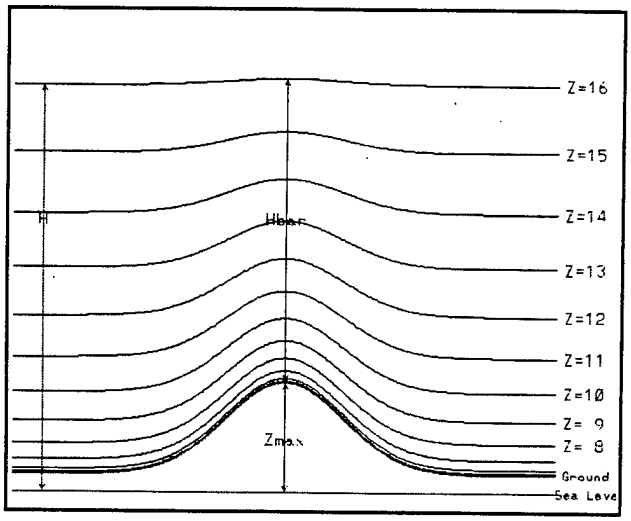

Figure 5. Model vertical level distribution over complex terrain.

Figure 5 shows the model vertical level distribution over complex terrain, showing that above a higher location, vertical layers are more densely packed. Layers near the surface are not shown.

Here,

z = the model level number.

The calculation of z* is $z^*(k)= c_1(k-0.5)^2 + c_2(k-0.5) + c_3$,

where

k = the level number,

and

c_1, c_2, and c_3 = constants determined within the model.

Figure 5 is a schematic presentation of how the BFM vertical layers are distributed over complex terrain. The layers are more densely packed over a high peak than over a low elevation point. More layers exist near the surface of the earth.

The following procedures are taken to analyze the data:

1. Horizontal wind components U' and V' (on the whole-mesh reference mesh of the GSM) are converted to U and V, where U and V are (respectively) the east-west and the north-south components of horizontal wind vectors.

By defining

$$\lambda' = 2\pi - [(\pi/180)\cdot 80 + \lambda] \tag{7}$$

where

λ = the longitude of the GSM grid (positive for the eastern hemisphere).
U and V are calculated by:

$$U = U'\cdot\cos\lambda' - V'\cdot\sin\lambda' \tag{8}$$

$$V = U'\cdot\sin\lambda' + V'\cdot\cos\lambda' . \tag{9}$$

2. Water vapor mixing ratio, Q_v, at the pressure level, P, is calculated from dew point temperature:

$$Q_v = 0.622\frac{e}{P} \tag{10}$$

$$e=6.11\exp[\frac{17.27T_d}{T_d+237.3}] \tag{11}$$

where

T_d = the dew point temperature in °C calculated as $T_d = T - \Delta$,

Δ = the dew point depression,

e = the saturation vapor pressure at the temperature T_d,

and

P = the pressure.

Virtual temperature, T_v, is calculated as:

$$T_v = T\,(1 + 0.61Q_v). \tag{12}$$

3. The parameters, U, V, T, Q_v and Φ on pressure levels are horizontally interpolated to the BFM horizontal grid points by the following method. A first guess value of a parameter Ψ at a grid point (i, j) is calculated as:

$$\Psi(i,j)=\frac{\sum_N \Psi_N \exp(-\frac{r_{ij,N}^2}{4k})}{\sum_N \exp(-\frac{r_{ij,N}^2}{4k})} \tag{13}$$

Here

Ψ = any parameter,

exponential function = the Barnes's weighting function, [3]

$r_{ij,N}$ = the normalized distance between a grid point (i, j) and the Nth GSM point,

and

k = an empirical parameter to determine the shape of the weighting function.

By using the first-guess values of the four grid points surrounding the Nth GSM point, an interpolated value at that point, Ψ'_N , is bilinearly calculated as:

$$t_1 = \Psi(x, y) + (x' - x)\cdot[\Psi(x + 1, y) - \Psi(x, y)] \quad (14)$$

$$t_2 = \Psi(x, y+1) + (x' - x)\cdot[\Psi(x + 1, y + 1) - \Psi(x, y + 1) \quad (15)$$

$$\Psi'_{N=} t_1 + (y' - y)\cdot[t_2 - t_1]. \quad (16)$$

Here,

(x,y) = the southwest grid of four grid points surrounding the Nth GSM point located at (x',y').

In figure 6,

" * " = the locations of GSM data points.

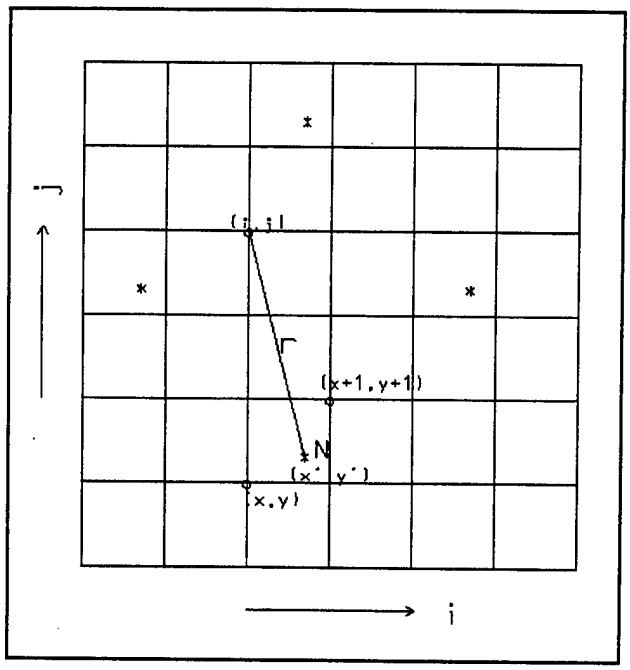

Figure 6. Schematic diagram showing the relationships between the BFM grid points and GSM data points.

The difference between the GSM value Ψ_N and Ψ'_N, $\Delta_N = \Psi_N - \Psi'_N$, is now distributed to the BFM grid points as:

$$\Delta(i,j) = \frac{\sum_N \Delta_N \exp(-\frac{r_{ij,N}^2}{4\gamma})}{\sum_N \exp(-\frac{r_{ij,N}^2}{4\gamma})} \qquad (17)$$

where

γ = an empirical weight reduction factor (0.2).

A final interpolated value of Ψ at (i, j), $\Psi_f(i, j)$ is calculated as:

$$\Psi_f(i, j) = \Psi(i, j) + \Delta(i, j) . \tag{18}$$

4. The parameter Ψ on pressure surfaces are linearly interpolated to z* level of the BFM as:

$$\Psi(z^*)=\Psi_k+\frac{\Psi_{k+1}-\Psi_k}{\phi_{k+1}-\phi_k}(z_{st}-\phi_k) \tag{19}$$

where

z_{st} = the Cartesian height above sea level of z*, calculated from equation (6) as:

$$z_{st}=z_g+z^*\frac{(\overline{H}+z_{gmax}-z_g)}{\overline{H}} \tag{20}$$

5. The surface pressure distribution over a complex terrain is determined as follows. If the terrain height z_g is between the pressure surfaces P_1 and P_2 ($P_1 > P_2$) where the geopotential heights and the temperature are, respectively, ϕ_1 and ϕ_2, ($\phi_1 < \phi_2$) and T_1 and T_2, the surface pressure is calculated using the hypsometric equation as:

I) $z_g - \phi_1 \leq \phi_2 - z_g$

$$P_{gr}=P_1\exp[\frac{g}{R_d\overline{T}}(z_g-\phi_1)] \tag{21}$$

where

$$\overline{T}=T_1+\frac{T_2-T_1}{\phi_2-\phi_1}(\overline{Z}_s-\phi_1) \tag{22}$$

and

$$\overline{Z}=\frac{1}{2}(z_g+\phi_1) \tag{23}$$

$$Zg-\Phi 1\geq \Phi 2-Zg$$

ii) $Z_g-\phi_1\geq \phi 1_2-Z_g$

$$P_{gr}=P_2\exp[\frac{g}{R_d\overline{T}}(\phi_2-z_g)] \tag{24}$$

where

$$\overline{T}=T_1+\frac{T_2-T_1}{Z_2-Z_1}(\overline{Z}-Z_1) \tag{25}$$

and

$$\overline{Z}=\frac{1}{2}(z_g+\phi_2) \tag{26}$$

3.2 Upper Air Sounding Data

Prior to the three-dimensional objective analysis, a quality control of upper air sounding data is made. The following criteria are applied to each sounding data:

- Flag the geopotential height values if the values differ by 15 percent or more from the standard atmosphere for pressure levels between 500 and 880 mb, and differ by 20 percent or more from the standard atmosphere for pressure levels below 880 mb. This check is not done at the first two levels above the surface.

- Flag the height of the second level if an extremely small pressure gradient (<0.02 mb/m) near the surface is found.

- Eliminate all layers with extreme temperature inversions ($\Delta T/\Delta z$ > 4°C/ 100 m), except near the surface. If such an inversion exists, a lower level is flagged. Near the surface, an inversion as extreme as 400°C/km is allowed.

- Eliminate extremely-superadiabatic layers ($\Delta T/\Delta z \leq$ -22°C/100 m) by flagging the lower level, except near the surface where lapse rates less than the autoconvective lapse rate (- g/R_d = -3.42°C/100 m) are allowed. Those critical values in the above are arbitrary, but seem to be not too unrealistic. More rigid criteria seem to often eliminate valid temperature data from observed data which could be of importance to modeling the boundary layer.

- Eliminate vertical wind speed shears exceeding 150 kn/km by flagging both levels.

- Correct duplicate pressure levels or heights/pressure out of order.

- Edit the data manually from the GUI window.

After the above steps, check the height fields by using the hypsometric equation.

After the above quality control, take the following procedures to produce three-dimensional data fields from the upper air sounding data:

- At each sounding location, parameters such as horizontal wind vector components, potential temperature, and water vapor mixing ratio are vertically interpolated to 20 different height levels (z_i, ASL) by using a linear interpolation method.

- At each z_i level, horizontal interpolation to the BFM grid is performed by using the weighting factor, $1/r^2$, as:

$$\Psi(i,j)=\frac{\sum_N \frac{\Psi_N}{r_{ij,N}^2}}{\sum_N \frac{1}{r_{ij,N}^2}} \qquad (27)$$

The weighting factor $1/r^2$ is used here. According to our experience, for a small number of observations, the Barnes method does not seem to produce reasonable fields.

- Linear vertical interpolation from z_i to z_{st}, given by equation (20) is performed for each parameter.

- The pressure values at H_{crit} m height ASL, $P_{Hcrit,N}$ at the sounding site N is calculated for each sounding site. The horizontal distribution at H_{crit} m level, $P_{Hcrit}(I, j)$ is calculated by using the weighting factor $1/r^2$. The level of H_{crit} m is chosen so that almost all sounding data have observed values. H_{crit} can be either 100, 500, 1000, 1500, 2500, or 3000 m ASL, and is determined from the available radiosonde site elevations.

- The difference of pressure between $P_{Hcrit,N}$ and the nearest grid value of P_{hcrit}, $\Delta_{N,}$ is redistributed horizontally to grid points by using the same weighting factor, and the new pressure values at H_{crit} m level, $P_{Hcrit,}$ are calculated as:

$$P_{Hcrit}(i,j)=P_{Hcrit}(i,j)+\frac{\sum_N \frac{\Delta_N}{r^2_{ij,N}}}{\sum_N \frac{1}{r^2_{ij,N}}} \tag{28}$$

- The surface pressure P_{grnd} is calculated from P_{Hcrit} by using the hypsometric equation:

$$P_{GRND}(i,j)=P_{Hcrit}(i,j)\exp[\frac{g}{R_d\overline{T}}\pm(H_{crit}-z_g(i,j))] \tag{29}$$

where

$\overline{T}$ = the average absolute temperature between z_g and H_{crit} m level, and inside the exponential,

and

+ sign = z_g below H_{crit} meters ASL

- sign = z_g above H_{crit} meters ASL.

3.3 Compositing the GSM and Upper Air Sounding Data

When both the GSM data and upper air sounding data are available, three-dimensional fields of the parameters composited from both data sources are usually used to initialize the BFM. The following procedures are taken to composite the two different data:

- Three-dimensional fields of the parameters (virtual potential temperature, dew-point temperature, horizontal wind components, u and v) are obtained from the GSM data on 20 vertical layers, z_i.

- Upper air sounding data is also interpolated to the 20 vertical layers, z_i.

- Three-dimensional data fields created from the GSM data are now used as background fields, $\Psi_G(i, j)$, and composited with the upper air sounding data, Ψ_U. Let's define the mean difference, $\overline{d}$ as:

$$\overline{d} = \frac{\sum_{N=1}^{N} (\Psi_{G,N} - \Psi_{U,N})}{N} \qquad (30)$$

where

$\Psi_{G,N}$ is the interpolated value to the Nth upper-air location by using the four-surrounding grid points, and $\Psi_{U,N}$ Nth upper-air data.

A bilinear interpolation method described in equations (14), (15) and (16) is used to calculate $\Psi_{G,N}$.

By replacing $\Psi_G(i, j)$ by

$$\Psi^*_G(i, j) = \Psi_G(i, j) + \overline{d} \tag{31}$$

the mean error is removed, but the values of $\Psi^*_{M,N}$ interpolated from $\Psi^*_G(i, j)$ for the Nth upper air location are not generally equal to $\Psi_{U,N}$.

The difference

$$d^*_N = \Psi_{U,N} - \Psi^*_{G,N} \tag{32}$$

is not zero, but the mean d^* is:

$$\overline{d^*} = \frac{\sum_{N=1}^{N} d^*_N}{N} = 0 \tag{33}$$

The next step is to distribute d^* to the entire field using a weighting function of $1/r^2$ as:

$$\Psi^{**}_G(i,j) = \Psi^*_G(i,j) + \frac{\sum_{N=1}^{N} \frac{d^*_N}{r^2_{ij,N}}}{\sum_{N=1}^{N} \frac{1}{r^2_{ij,N}}} \tag{34}$$

The above procedures are applied to all vertical levels, z_i, for all the parameters, and vertical linear interpolation from z_i to z^* are performed. Linear interpolation from z_i levels to z_{st} are performed for all the parameters, and dew-point temperature field is converted to water vapor mixing ratio field by using the formula given in equation (11).

For surface pressure calculations, the observed surface pressure values are corrected to the model elevation by using the hyposometric equations because the radiosonde site elevations and the model elevations for the corresponding locations are generally different. The corrected observed values are composited by using the above procedures.

4. Forecast Model

For forecast calculations, the BFM uses a mesoscale model (HOTMAC) developed by Yamada. [4] This model is based on a set of second-moment turbulence equations closed by assuming certain relationships between unknown higher-order turbulence moments, and the known lower-order moments. The model output variables are wind, potential temperature, the mixing ratios of water vapor and cloud water, turbulence second moments, a turbulence length scale, and turbulence transport coefficients (eddy viscosity and eddy diffusivity). The model is time dependent and three-dimensional in space.

HOTMAC can be used under quite general conditions of flow and thermal stratification. Methods for turbulence parameterization are more advanced than those in simple eddy viscosity models. This model, combined with a statistical cloud model, can simulate interaction between water phase changes and basic dynamic variables. Effects of short and long-wave solar radiation, and topography are also included in the model. Surface temperature is computed from a heat conduction equation for the soil, and a heat energy balance equation at the surface.

The model assumes hydrostatic equilibium and uses the Boussinesq approximation. Under the Boussinesq approximation, it is assumed that the modeled fluid is incompressible to the extent that thermal expansion produces a buoyancy. Buoyancy forces are retained in a hydrostatic basic state with respect to pressure and density via the inclusion of small pressure and density deviations. This assumption holds as long as the density deviation from the mean state is negligible. The density variations are only considered when they are closely coupled to gravity. Therefore, in theory, the model applications are limited to flows where the local acceleration and advection terms in the equation of vertical motion are much smaller than the acceleration due to gravity (hydrostatic

equilibrium) and temperature variations in the horizontal directions are not too large.

The content of this chapter is mainly summarized from publications by Yamada. [3], [4] , [5] Some modifications are made to the original source code, and noted in the text.

4.1 Governing Equations

A terrain following vertical coordinate system is used to increase the accuracy in the treatment of surface boundary conditions equation (6). Following a coordinate transformation [5], the governing equations are given by:

$$\frac{DU}{Dt}=f(V-V_g)+g\frac{\overline{H}-z^*}{\overline{H}}\left(1-\frac{\langle\theta_v\rangle}{\theta_v}\right)\frac{\partial z_g}{\partial x}+\frac{\partial}{\partial x}\left(K_x\frac{\partial U}{\partial x}\right)+\frac{\partial}{\partial y}\left(K_{xy}\frac{\partial U}{\partial y}\right)+\frac{\overline{H}}{H-z_g}\frac{\partial}{\partial z^*}\left(-\overline{uw}\right) \tag{35}$$

$$\frac{DV}{Dt}=-f(U-U_g)+g\frac{\overline{H}-z^*}{\overline{H}}\left(1-\frac{\langle\theta_v\rangle}{\theta_v}\right)\frac{\partial z_g}{\partial y}+\frac{\partial}{\partial y}\left(K_y\frac{\partial V}{\partial y}\right)+\frac{\partial}{\partial x}\left(K_{xy}\frac{\partial V}{\partial x}\right)+\frac{\overline{H}}{H-z_g}\frac{\partial}{\partial z^*}\left(-\overline{vw}\right) \tag{36}$$

where

$$\frac{\partial U}{\partial x}+\frac{\partial V}{\partial y}+\frac{\partial W^*}{\partial z^*}-\frac{1}{H-z_g}\left(U\frac{\partial z_g}{\partial x}+V\frac{\partial z_g}{\partial y}\right)=0 \tag{37}$$

$$W^*\equiv\frac{\overline{H}}{H-z_g}W+\frac{z^*-\overline{H}}{H-z_g}\left(U\frac{\partial z_g}{\partial x}+V\frac{\partial z_g}{\partial y}\right) \tag{38}$$

and

$$\frac{D()}{Dt}=\frac{\partial()}{\partial t}+U\frac{\partial()}{\partial x}+V\frac{\partial()}{\partial y}+W^{*}\frac{\partial()}{\partial z^{*}} \tag{39}$$

In the above expressions, $<\theta_v>$ is the base state virtual potential temperature, which we are defining as the initial virtual potential temperature field obtained by the three-dimensional objective analysis of input data. The perturbation potential temperature field is defined as the change from this base state over time. Due to this approach, in cases with very strong frontal zones and very large temperature gradients, the Boussinesq approximation may lose some of its validity. The second terms on the right-hand side of equations (33) and (34) and the fourth term of equation (35) express the effects of ground slope.

In the original code of the HOTMAC, the geostrophic winds U_g and V_g are computed by:

$$fU_g \equiv fU_g(\overline{H})\frac{<\Theta_v>}{<\Theta_v(\overline{H})>}+g\frac{H-z_g}{\overline{H}}\int_z^{\overline{H}}\frac{1}{<\Theta_v>}\frac{\partial}{\partial y}\delta\Theta_v dz'-\frac{g}{\overline{H}}\frac{\partial z_g}{\partial y}\int_z^{\overline{H}}\frac{\delta\Theta_v}{<\Theta_v>}dz' \tag{40}$$

$$fV_g \equiv fV_g(\overline{H})\frac{<\Theta_v>}{<\Theta_v(\overline{H})>}-g\frac{H-z_g}{\overline{H}}\int_z^{\overline{H}}\frac{1}{<\Theta_v>}\frac{\partial}{\partial x}\delta\Theta_v dz'+\frac{g}{\overline{H}}\frac{\partial z_g}{\partial x}\int_z^{\overline{H}}\frac{\delta\Theta_v}{<\Theta_v>}dz' \tag{41}$$

where

$$\delta\Theta_v=\Theta_v-<\Theta_v>,$$

and the abbreviated symbols

$$U_g(\overline{H})=U_g(x, y, \overline{H}, t)\,,$$

and

$$V_g(\overline{H})=V_g(x, y, \overline{H}, t)$$

are used.

In deriving equations (38) and (39), Yamada makes several assumptions, the most substantial being that $<\Theta_v>$ is independent of height z. [5] Based on our definition of $<\Theta_v>$, this is only a valid asssumption in the lowest 1 to 2 km AGL. It is invalid for the BFM since its model top is at 7000 m AGL or greater. However, by eliminating this assumption, we have detected that equations (38) and (39) produce unrealistically extreme magnitudes of geostrophic wind speeds, particularly over complex terrain. This is due to the problem of trying to resolve the difference between two very large terms of opposite sign, needed to compute the pressure gradient in the z^* coordinate system. To avoid this, the following approach has been taken:

- The values of $<\Theta_v(\overline{H})>$, $U_g(\overline{H})$, and $V_g(\overline{H})$ in equations (38) and (39) are replaced by the values at the grid point vertical level nearest to 1500 mAGL, z_{crit}.

- Below level z_{crit}, solve for U_g and V_g using equations (38) and (39) and the substitutions mentioned above in 1.

- At, and above level z_{crit} U_g and V_g are set equal to the smoothed model generated grid point wind value, using the four surrounding grid points and a smoothing factor of 0.5. At the lateral boundaries the same scheme is applied, except that the three surrounding grid points are used.

The above process eliminates the false generation of extreme U_g and V_g wind components , and allows the large-scale geostrophic components to stay in line with the large-scale GSM guidance. At the same time, it allows the geostrophic components in the lower boundary layer to be determined by the pressure gradient force (using thermal wind principles in the layer z^* to z_{crit} and the model perturbation virtual potential temperature field) generated by the BFM surface physics. The geostrophic wind calculating scheme may be modified in the future.

A turbulence kinetic energy equation is given by:

$$\frac{D}{Dt}(\frac{q^2}{2})=\frac{\partial}{\partial x}[K_x\frac{\partial}{\partial x}(\frac{q^2}{2})]+\frac{\partial}{\partial y}[K_y\frac{\partial}{\partial y}(\frac{q^2}{2})]$$

$$+(\frac{\overline{H}}{H-z_g})^2\frac{\partial}{\partial z^*}[qlS_q\frac{\partial}{\partial z^*}(\frac{q^2}{2})]$$

$$-\frac{\overline{H}}{H-z_g}(\overline{uw}\frac{\partial U}{\partial z^*}+\overline{vw}\frac{\partial V}{\partial z^*})+\beta g\overline{w\theta_v}-\frac{q^3}{B_1 l} \qquad (42)$$

a turbulence length scale l is obtained from:

$$\frac{D}{Dt}(q^2 l)=\frac{\partial}{\partial x}[K_x\frac{\partial}{\partial x}(q^2 l)]+\frac{\partial}{\partial y}[K_y\frac{\partial}{\partial y}(q^2 l)]$$

$$+(\frac{\overline{H}}{H-z_g})^2\frac{\partial}{\partial z^*}[qlS_l\frac{\partial}{\partial z^*}(q^2 l)]$$

$$-lF_1[\frac{\overline{H}}{H-z_g}(-\overline{uw}\frac{\partial U}{\partial z^*}-\overline{uw}\frac{\partial V}{\partial z^*})+\beta g\overline{w\theta_v}]$$

$$-\frac{q^3}{B_1}[1+F_2(\frac{l}{kz})^2] \qquad (43)$$

where

q^2 = twice the turbulence kinetic energy defined as:

$$q^2=\overline{u^2}+\overline{v^2}+\overline{w^2} \qquad (44)$$

where

$w\theta_v$ = turbulence heat flux,

θ_v = the fluctuation part of virtual potential temperature,

and

$(F_1, F_2, S_q, S_l, B_l)=(1.8, 1.33, 0.2, 0.2, 16.6.)$.

These empirical constants were determined from laboratory experiments [7] for neutral boundary layer flow, and are applied, in the BFM, to other atmospheric stability cases. The internal heat energy equation is written as:

$$\frac{D\delta\Theta_v}{Dt}=\frac{\partial}{\partial x}[K_x\frac{\partial\Theta_v}{\partial x}]+\frac{\partial}{\partial y}[K_y\frac{\partial\Theta_v}{\partial y}]+\frac{\overline{H}}{H-z_g}$$

$$\cdot[\frac{\partial}{\partial z^*}(-\overline{w\theta})+\frac{1}{\rho C_p}\frac{\partial R_N}{\partial z^*}-W\frac{\partial\Theta\theta_v}{\partial z}] \qquad (45)$$

The long-wave radiation flux $R_N/\rho C_p$ is computed according to Sasamori. [8] A conservation equation for the mixing ratio of total water ($Q_w=Q_v + Q_c$) is given by

$$\frac{DQ_w}{Dt}=\frac{\partial}{\partial x}[K_x\frac{\partial Q_w}{\partial x}]+\frac{\partial}{\partial y}[K_y\frac{\partial Q_w}{\partial y}]+\frac{\overline{H}}{H-z_g}\frac{\partial}{\partial z^*}(-\overline{wq_v}) \qquad (46)$$

where

Q_v = the mixing ratio of water vapor

and

Q_c = the mixing ratio of cloud water.

The turbulent fluxes in equations (33), (34), (41), (42), (43), and (44) are obtained from simplified, second-moment, turbulence-closure equations, [9]

$$(\overline{uw},\overline{vw}) = -lqS_M[\frac{\partial U}{\partial z},\frac{\partial V}{\partial z}] \quad (47)$$

$$(\overline{w\theta},\overline{wq_v}) = -\alpha lqS_M[\frac{\partial \theta}{\partial z},\frac{\partial Q_v}{\partial z}] \quad (48)$$

where

S_M and α = functions of the flux Richardson number.

α is the reciprocal of the turbulent Prandtl number and given by K_H/K_M

where

K_H = an eddy diffusivity coefficient

and

K_M = an eddy viscosity coefficient.

The final expressions for S_M and α are given in Yamada [9] as:
for $Ri_f<0.16$

$$S_M = 1.96\frac{(0.1912 - Ri_f)(0.2341 - Ri_f)}{(1 - Ri_f)(0.2231 - Ri_f)} \quad (49)$$

and for $Ri_f \geq 0.16$,

$$S_M = 0.085 \tag{50}$$

$$\alpha = 1.318 \frac{0.2231 - Ri_f}{0.2341 - Ri_f} \qquad Ri_f < 0.16 \tag{51}$$

$$= 1.12 \qquad Ri_f > 0.16$$

The relationship between the gradient Richardson number

$$Ri_g = \frac{g \partial \theta / \partial z}{\theta (\partial U / \partial z)^2} \tag{52}$$

and the flux Richardson number

$$Ri_f = \frac{g \overline{w\theta}}{\theta [\overline{uw} \partial U / \partial z + \overline{vw} \partial V / \partial z]} \tag{53}$$

is given by:

$$Ri_f = 0.6588 (Ri_g + 0.1776 - [Ri^2 - 0.3221 Ri + 0.03156]^{1/2})$$

for $R_{ig} < R_{ic} = R_{ifc}$ for $R_{ig} \geq R_{ic}$

where

Ri_{fc} (=0.191) = a critical flux Richardson number

and

Ri_c (=0.195) = a critical gradient Richardson number.

4.2 Surface Boundary Conditions

Surface boundary conditions for equations (35), (36), and (42) through (46) are constructed from the empirical formulas by Dyer and Hicks for the nondimensional wind and temperature profiles as follows: [10]

$$\frac{V(z)}{u_*}=\frac{1}{k}[\ln(z+z_0)/z_0-\Psi_m(\zeta)] \tag{55}$$

$$\frac{\theta(z)-\theta(0)}{T_*}=\frac{P_r}{k}[\ln(\frac{z+z_{0t}}{z_{0t}})-\Psi_h(\zeta)] \tag{56}$$

$$\frac{Q_v(z)-Q_v(0)}{Q_*}=\frac{S_c}{k}[\ln(\frac{z+z_{0v}}{z_{0v}})-\Psi_v(\zeta) \tag{57}$$

$$q^2(z)=B_1^{2/3}u_*^2(\Phi_m-\zeta)^{2/3} \tag{58}$$

$$q^2l(z)=kzq^2(z) \tag{59}$$

In the above equations, V(z), Θ(z) and $Q_v(z)$ are abbreviations for V(x,y,z,t), Θ (x, y, z, t), and Q_v(x, y, z, t), respectively, and V(z) is the horizontal wind speed. Terms u_*, T_*, and Q_*, defined as $u_*=(\tau/\rho)^{1/2}$, $T_*=H/\rho c_p u_*$, and $Q_*= E/\rho u_*$, are friction velocity and scales for temperature and water vapor, respectively. τ, H, and E are surface stress, total sensible heat, and rate of evaporation, respectively. Total sensible heat is defined as:

$$=\overline{w\theta_v}=(1+0.61Q_w)\overline{w\theta}+0.61\overline{w\theta} \tag{60}$$

and the Monin-Obukhov length, L, is:

$$L=-u_*^3/k\beta gH \tag{61}$$

The parameter

ζ = a nondimensional height z/L;

k = the von Karman constant;

z_0, z_{0t}, and z_{0v} = roughness lengths for wind, temperature, and water vapor;

and

P_r and S_c = turbulence Prandtl and Schmidt numbers, respectively.

Terms

Ψ_m, Ψ_h, and Ψ_v [11] = correction terms for the atmospheric stability.

Their functional forms are given by:

$$_m(\zeta)=\int_0^{\zeta}\frac{1-\phi_m(\zeta')}{\zeta'}d \tag{62}$$

$$\Psi_h(\zeta)=\int_0^{\zeta}\frac{1-\phi_h(\zeta')}{\zeta'}d\zeta' \tag{63}$$

$$\Psi_v(\zeta)=\int_0^{\zeta}\frac{1-\phi_v(\zeta')}{\zeta'}d\zeta' \tag{64}$$

where

ϕ_m, ϕ_h, and ϕ_v = nondimensional wind, temperature, and water vapor gradients.

The following formulations [10] are used for ϕ_m, ϕ_h, and ϕ_v under unstable conditions:

$$\phi_m(\zeta)=(u_*/kz)(\partial U/\partial z)=(1-15\zeta)^{-1/4} \tag{65}$$

$$\phi_h(\zeta)=(T_*/kz)(\partial\theta/\partial z)=(1-15\zeta)^{-1/2} \tag{66}$$

$$\phi_v(\zeta)=(Q_*/kz)(\partial Q_v/\partial z)=(1-15\zeta)^{-1/2} \tag{67}$$

For stable conditions,

$$\phi_m(\zeta)=\phi_h(\zeta)=\phi_v(\zeta)=1+5\zeta \tag{68}$$

The above formulas are valid only for horizontally homogeneous surfaces. However, it is assumed that the same relations are fair approximations over nonhomogeneous terrain, provided that the formulas are applied sufficiently close to the surface. Vegetation plays an active part in the apportionment of available heat energy between convective (sensible and latent) and conductive (into soil) components. HOTMAC has a parameterization scheme of tall tree effects, but in the current BFM it is assumed that an entire model domain is covered with bare soil. In the future, the parameterization of vegetation cover will be included in the model.

In the model, the distinctions between land and water are made in surface roughness parameters and surface temperature. Over land, z_0 and z_{0t} ($=z_{0v}$) are, respectively, 0.1 and 0.0135 m. Over water, $z_0=0.016u_*^2/g$, and $z_{0t} = z_{0v} = 0.000022/ku$. Surface temperature over land is calculated from the surface energy balance. Temperature over water is assumed to stay constant during a forecast period at the values determined from the climatological monthly average temperatures.

4.3 Surface Energy Balance and Surface Temperature

Use of the similarity formulas requires knowledge of surface temperatures. The temperature T_s in the soil layer is obtained by solving the heat conduction equation:

$$\frac{\partial T_s}{\partial t}=\frac{\partial}{\partial z_s}(K_s\frac{\partial T_s}{\partial z_s}) \tag{69}$$

where

z_s = positive downward,

and soil heat conductivity K_s can be a function of soil moisture content and emissivity ϵ. Appropriate boundary conditions for solution of equation (69) are the heat energy balance at the soil surface and specification of the soil temperature at a certain depth. The heat energy balance at the surface is given by:

$$R_s + R_L\uparrow - R_L\downarrow = H_s + LE + G_s \tag{70}$$

where

R_s = the incoming direct solar radiation absorbed by the surface,
$R_L\downarrow$ = the incoming long-wave radiation,

and

$R_L\uparrow$ = the outgoing long-wave radiation.

In this model, the loss of direct solar radiation due to the absorption by cloud and the small effects of the earth's annual orbital changes are taken into consideration, but the contribution of diffuse solar radiation is not. The sensible heat flux H_s, latent heat flux LE, and ground heat flux G_s are given by:

$$H_s = -\rho_a C_p u_* T_* \tag{71}$$

$$LE = -\rho\, L u_* Q_* \tag{72}$$

$$G_s = K_s \frac{\partial T_s}{\partial z_s}\Big|_G \tag{73}$$

where

ρ = the air density,
u_* = the friction velocity,
T^* = the temperature scale,
Q_* = the water vapor scale,

and

subscript G = the value at the ground surface.

Substituting equation (68) to (70) into (67), we obtain:

$$R_s + \epsilon R_L\downarrow - \epsilon\sigma T^4_G = -\rho_a C_p u_* T_* - \rho_a L u_* Q_* - K_s(\partial T_s/\partial z_s)|_G \qquad (74)$$

where

$$R_L\uparrow = \epsilon\sigma T^4_G + (1 - \epsilon)R_L\downarrow \qquad (75)$$

is used,

ϵ = the emissivity of the surface,
σ = the Stefan-Boltzman constant.

Garratt and Hicks [12] obtained a relationship between the surface temperature and air temperature at z_1 in the surface layer:

$$\frac{\theta(z_1)-\theta_G}{T_*} = \frac{P_r}{k}\left[\ln\frac{z_1+z_{0t}}{z_0} + \ln\frac{z_0}{z_{0t}} - \Psi_h(\zeta)\right] \qquad (76)$$

A constant value of 0.1 m is assumed for z_0, and z_{0t} is obtained from a relationship $\ln(z_0/z_{0t})=2$. [12] Using equation (56) we can eliminate T_* from equation (74) to obtain:

$$R_s+\epsilon R_L{\downarrow}-\epsilon\sigma T_G{}^4+m[\theta(z_1)-T_G(P_0/P_G)^{R/C_p}]+K_s(\frac{\partial T_s}{\partial z_s})|_G=0 \qquad (77)$$

where

$$m=k\rho_a C_p u_*(1+B^{-1})P_r{}^{-1}[\ln(\frac{z_1+z_{0t}}{z_0})+2-\Psi_h(\zeta)] \qquad (78)$$

P_0 = a reference pressure (1000 mb)

P_G = the pressure at the surface.

Equation (77) can be linearized by noting that

$$\frac{T_G{}^{n+1}-T_G{}^n}{T_G{}^n}\ll 1 \qquad (79)$$

where

n and n+1 = the n and $(n+1)^{th}$ time steps of integration (a typical time increment used in integration is 1 to 10 min).

After substitution into equation (77) of the approximation

$$(T_G{}^{n+1})^4\approx 4(T_G{}^n)^3 T_G{}^{n+1}-3(T_G{}^n)^4 \qquad (80)$$

we obtain:

$$[4\epsilon\varepsilon\sigma(T_G{}^n)^3+m(\frac{P_0}{P_G})^{R/c_p}+\frac{K_s}{\Delta z_s}]T_G{}^{n+1}$$

$$=(\frac{K_s}{\Delta z_s})T_s{}^{n+1}(1)+R_s+\epsilon R_L{\downarrow}+3\epsilon\varepsilon\sigma(T_G{}^n)^4+m\theta^n(z_1) \qquad (81)$$

where the derivative $\partial T_s/\partial z_s|_G$ is replaced by a forward finite-difference approximation,

$(T_s{}^{n+1}(1) - T_G{}^{n+1})/\Delta z_s$; $T_s(1)$ = the soil temperature at the first grid level from the surface;

and

Δz_s = the distance between the surface and the first grid level in the soil layer.

By this method, equation (69) is solved numerically in finite-difference form by the Laasonen method. [13] By this method, equation (69) reduces to $AT_s=B$

where

A = a tridiagonal matrix

and

B = a column vector.

The solution is conveniently obtained by using the relation:

$$(T_s)_l = E_l(T_s)_{l+1} + F_l \tag{82}$$

where

$(T_s)_l$ = the soil temperature at the l^{th} grid level from the surface.

Expressions for E_l and F_l for $l > 1$ are determined from the finite-difference form of equation (69), and equation (81) determines E_l and F_l. From equations (81) and (82), we obtain:

$$E_l = \frac{(\frac{K_s}{\Delta z_s})}{4\varepsilon\sigma(T_G^n)^3 + m(\frac{P_0}{P_G})^{R/C_p} + \frac{K_s}{\Delta z_s}} \tag{83}$$

and

$$F_l = \frac{[R_s + \varepsilon\sigma(T_G^n)^4 + m\theta^t(z_l)]}{4\varepsilon\sigma(T_G^n)^{R/C_p} + m(\frac{P_0}{P_G})^{R/C_p} + (\frac{K_s}{\Delta z_s})} \tag{84}$$

Numerical integration of equation (69) by use of equations (82) through (84) is rapid since no iteration is required.

4.4 Radiational Energy Fluxes

The incoming direct solar radiation flux to an inclined surface is obtained from Kondratyev: [14]

$$R_s = R_0[A + B\cos\Omega + C\sin\Omega]\left(\frac{a^2}{r^2}\right) \quad (85)$$

where

$$a^2/r^2 = 1.000110 + 0.034221\cos(\theta_0) + 0.001280\sin(\theta_0) + 0.000719\cos(2\theta_0) + 0.000077\sin(2\theta_0) \quad (86)$$

and

$$\theta_0 = 2\pi J_d/365 \quad (87)$$

$$A = \cos\alpha\sin\Phi\sin\delta + \sin\alpha[\cos\Psi_n(\tan\Phi\sin\Phi\sin\delta - \sin\delta\sec\Phi)] \quad (88)$$

$$B = \cos\alpha\cos\Phi\cos\delta + \sin\alpha\cos\Phi\sin\Psi_n\cos\delta \quad (89)$$

and

$$C = \sin\alpha\cos\delta\sin\Psi_n \quad (90)$$

In the above expressions,

R_0 = the near surface, direct solar radiation flux;
Ω = the solar hour angle (positive clockwise from apparent noon);
Φ = the latitude;
δ = the declination of the sun;
α = the angular inclination of the surface to the horizontal plane;

and

Ψ_n = the azimuth of the projection of the normal to the surface on the horizontal plane, as counted from the plane of the meridian (azimuth is considered positive when counted clockwise).

Because the maximum change in the solar declination δ in 24 h is less than 0.5°, δ is assumed to be constant during a given day. Paltridge and Platt [15] provide a formula to compute δ in rads by:

$$\begin{aligned}\delta = {} & 0.006918 - 0.399912\cos\theta_0 + 0.070257\sin\theta_0 \\ & - 0.006758\cos 2\theta_0 + 0.000907\sin 2\theta_0 \\ & - 0.002697\cos 3\theta_0 + 0.001480\sin 3\theta_0. \end{aligned} \quad (91)$$

Equation (91) estimates δ with a maximum error of 0.0006 rd. Solar hour Ω can be obtained if the longitude, clocktime, and the equation of time are known. The equation of time is the difference between the local apparent time and a fixed mean solar time, which is derived from the motion of a celestial equation at a rate equal to the average movement of the sun. The solar angle Ω is given in rads by:

$$\Omega = \frac{\pi(t_s - 12)}{12} \quad (92)$$

where

t_s = the true solar time (local apparent time) in hours.

The true solar time is obtained from:

$$t_s = t_{c.t.} + \Delta t_{long} + t_{eq} \tag{93}$$

where

$t_{c.t.}$, Δt_{long}, and t_{eq} = the clocktime, the longitude correction, and the equation of time.

The longitude correction accounts for the difference between the local meridian and a standard meridian, and is positive if the local meridian is east of standard. The equation of time is as follows: [15]

$$t_{eq} = \frac{12}{\pi}(0.000075 + 0.001868\cos\theta_0$$

$$-0.032077\sin\theta_0 - 0.014615\cos 2\theta_0 - 0.40849\sin 2\theta_0) \tag{94}$$

where

t_{eq} = hours

θ_0 = defined by equation (87).

Equation (94) has a maximum error, compared with values tabulated in the National Almanac, of 35 s in time. The amount of solar radiation reaching the surface is much less than that at the top of the atmosphere due to many factors, including molecular scattering and absorption by permanent gases such as oxygen, ozone, and carbon dioxide. The effect is parameterized by Atwater and Brown [16], who modified the original form by Kondratyev to include the effect of the forward Rayleigh scattering. [17]

The expression is:

$$G=0.485+0.515[1.041-0.16(\frac{0.000949P+0.051}{\cos\mu_0})^{1/2}] \quad (95)$$

where

P = the surface pressure in megabytes.

Other important factors that also modify the amount of incoming solar radiation include water vapor, clouds, and airborne particles. Parameterizations for clouds are described in section 4.8. Currently R_0 is calculated from:

$$R_0=R_{0s}G \quad (96)$$

where

R_{0s} = the incoming radiation flux at the top of the atmosphere

and G is given by equation (95). The zenith angle μ_0 in equation (95) is determined from:

$$\cos\mu_0=\sin\Phi\sin\delta+\cos\Phi\cos\delta\cos\Omega \quad (97)$$

Finally, $R_L\downarrow$, the long-wave incoming radiation at the surface, is computed according to the following formula:

$$R_L\downarrow = R_0\downarrow\cos\alpha \quad (98)$$

where

$R_0\downarrow$ = the long-wave incoming radiation normal to horizontal surface,

α = the angle of inclination of a sloped surface given by:

$$\alpha=\tan^{-1}[(\frac{\partial z_g}{\partial x})^2+(\frac{\partial z_g}{\partial y})^2]^{1/2} \quad (99)$$

When cloud is present in the model atmosphere, the surface fluxes of both short and long wave radiations are modified according to the methods described in section 4.8.

4.5 Upper Boundary Conditions

Boundary values for P, U, V, Θ_v,and Q_w, along the upper computational boundary, are given by the values yielded from the analysis of the GSM plus upper air sounding data. The values are updated hourly by linearly interpolating between the analysis fields at T_0, T_0 + 12 and T_0 + 24. Turbulence and vertical velocity are assumed to vanish along the upper boundary.

4.6 Lateral Boundary Conditions

The lateral boundary values for U, V, Θ_v, Q_w, q^2, and $q^2 l$ are obtained by integrating the corresponding governing equations (35), (36), (42), (43), and (45), except that variations in the horizontal directions are neglected. Variables U, V, Θ_v, Q_w, q^2, and $q^2 l$ are smoothed at each time step by using the values at four neighboring points, such as.:

$$\varphi_{i,j}=(1-\lambda)\varphi_{i,j}+0.25\lambda(\varphi_{i+1,j}+\varphi_{i-1,j}+\varphi_{i,j-1}\varphi_{i,j+1}) \quad (100)$$

where

φ = either U, V, Θ_v, Q_w, q^2, $q^2 l$,

λ = smoothing parameter (=0.25).

A similar expression, using only three neighboring points, is applied to the values at the lateral boundaries. In addition, changes have been made in the code that damp the effects of terrain slopes at the boundaries. This makes it possible to put the boundaries in very complex terrain without constructing an artificial apron around the model domain. Also, the model code forces the first grid vertical cell to be at 4 m AGL. This is to ensure that the lowest layer is sufficiently near the ground to generate appropriate slope flows.

4.7 Diagnostic Pressure Distribution

In the original code of HOTMAC, three-dimensional pressure distribution is diagnostically calculated at each time step from the initial distribution of pressure at the top of the model atmosphere and the three-dimensional temperature distribution that is calculated prognostically. However, we found that by this method the pressure distribution sometimes becomes unrealistic.

By using a time-dependent distribution of pressure at the top of the model atmosphere, as described in the following, a more dependable pressure distribution is obtained.

Initially, the surface pressure distribution is calculated from the GSM and upper air sounding data. Using this data, the three-dimensional pressure distribution over the model domain is calculated as follows. A modified pressure is defined as:

$$\Pi = C_p \left(\frac{P}{P_0}\right)^{\kappa} \tag{101}$$

where

P_0 = a reference pressure (1000 mb),

κ = the ratio,

C_p = the specific heat of the dry air at constant pressure,

R_d = gas constant of dry air.

The hydrostatic equation in Cartesian coordinates can be written as:

$$\frac{\partial \Pi}{\partial z} = -\frac{g}{\theta_v} \tag{102}$$

In the transformed coordinate,

$$\frac{\partial \Pi}{\partial z^*} = \frac{\partial \Pi}{\partial z}\frac{\partial z}{\partial z^*} = -g\frac{(H - z_g)}{\overline{H}\theta_v} \tag{103}$$

From equation (103), the modified pressure at the top of model atmosphere is calculated as:

$$\Pi(\overline{H}) = \Pi(0) - \frac{g(H - z_g)}{\overline{H}}\int_0^{\overline{H}} \frac{dz}{\theta_v} \tag{104}$$

where the modified pressure at the surface $\Pi(0)$ is calculated from a surface pressure value as:

$$\Pi(0) = C_p\left(\frac{P_{surf}}{P_0}\right)^{\kappa} \tag{105}$$

From the initial and boundary condition analyzed fields of the surface pressure from the GSM (and at initial time, the upper air sounding data as well), the modified pressure distribution at the top of the model atmosphere is calculated by using equation (101) at the initial , 12-, and 24-h forecast time. The modified pressure at the top of the model atmosphere at time t after the initialization for t less than 12 h is now calculated as:

$$\Pi(\overline{H})_t=\Pi(\overline{H})_0+\frac{\Pi(\overline{H})_{12}-\Pi(\overline{H})_0}{12}\bullet t \tag{106}$$

where the subscripts 0 and 12 stand for t=0 and 12 hours, respectively. A similar equation is used for t between 12 and 24 hours.

The modified pressure at the level z* at time t is calculated as:

$$\Pi(z^*)=\Pi(\overline{H})_t+\frac{(H-z_g)}{\overline{H}}\int_{z^*}^{\overline{H}}\frac{dz}{\theta_v}. \tag{107}$$

4.8 Radiative Effects in Clouds

Solar and longwave radiation play important roles in the formation and dissipation of clouds and fog. For example, radiation fog forms when moist air near the surface condenses as the ground temperature decreases due to longwave radiational cooling. As the sun rises, fog reflects, absorbs, and transfers shortwave radiation. The solar energy absorbed in a fog layer heats the air and converts liquid water to water vapor. The solar energy transmitted through fog heats the ground and increases ground temperature. The warmed ground, in turn, heats the air above and dissipates the fog. Interaction between radiative transfer and cloud

development is understood qualitatively. However, a quantitative description is complex and involves considerable computations. [18] [19]

Hanson and Derr proposed a parameterized solar radiation scheme whose parameters were obtained by curve-fitting to numerical radiative-transfer results using the atmospheric radiation (ATRAD) narrow band model. [20], [21] This parameterized method is simple, yet reproduced solar flux profiles within a single cloud layer that were in good agreement with the numerical results obtained from ATRAD.

Motivated by the success of the solar radiation scheme, Hanson and Derr proposed an infrared radiation scheme expressed by exponential functions whose decay parameters were determined by the emissive method. [22] This method reproduced infrared flux profiles within layered clouds that were in good agreement with the numerical results and observations for thick clouds (about 800 m). However, the parameterization overestimated the flux decrease at the cloud top and underestimated the cloud base warming compared to the numerical model for thin clouds (about 300 m).

The BFM has adopted the Hanson and Derr parameterization scheme because of simplicity and because it can produce flux profiles that are in good agreement with observations and numerical results. [23]

4.8.1 Shortwave Radiation

Following the two-stream model solutions by Stephens et al., reflection (R_c), transmission (T_r) and absorption (A_b) are expressed as: [24]

(1) Nonabsorbing medium [$\varpi_0 = 1$ ($\lambda \leq 0.75$ μm)]

$$R_e(\mu_0) = \frac{\beta(\mu_0)\tau_N/\mu_0}{1+\beta(\mu_0)\tau_N/\mu_0} \qquad (108)$$

$$T_r(\mu_0) = 1 - R_e(\mu_0) \tag{109}$$

(2) Absorbing medium [$\varpi_0 \leq 1$ ($\lambda \geq 0.75$ μm)]

$$R_e(\mu_0) = [(u^2 - 1)\exp(\tau_{eff}) - \exp(-\tau_{eff})]/R \tag{110}$$

$$T_r(\mu_0) = 4u/R \tag{111}$$

$$A_b(\mu_0) = 1 - R_e(\mu_0) - T_r(\mu_0) \tag{112}$$

where

$$u^2 = [1 - \varpi_0 + 2\beta(\mu_0)\varpi_0]/(1 - \varpi_0) \tag{113}$$

$$\tau_{eff} = \{(1 - \varpi_0)[1 - \varpi_0 + 2\beta(\mu_0)\varpi_0]\}^{1/2}\tau_N/\mu_0 \tag{114}$$

$$R = (u + 1)^2\exp(\tau_{eff}) - (u - 1)^2\exp(-\tau_{eff}) . \tag{115}$$

In the above expression,

μ_0 = the zenith angle,

τ_N = the optical thickness of the cloud,

ϖ_0 = the single-scattering albedo,

β = the backscattered fraction of monodirectional incident radiation.

The values for ϖ_0 and β are tabulated as functions of τ_0 and μ_0.

The solar radiation flux profile within the layered cloud is computed from the following equations: [20]

$$F(z)=F_B - (F_B - F_C)[1 - \exp(-(z_B - z)/\lambda_S)]/$$

$$\{1 - \exp[- (z_B - z_C)/\lambda_S]\} \quad (116)$$

where

$$\lambda_S = a(\mu_0)W + b(\mu_0)(1 - \exp\{ -[\gamma W + c(\mu_0)]) \quad (117)$$

$$F_C = F_B + A_b F_B\downarrow \quad (118)$$

$$a(\mu_0) = -0.022 + 0.038(1 - \mu_0) \quad (119)$$

$$b(\mu_0) = 56.8 - 14.7(1 - \mu_0) \quad (120)$$

$$c(\mu_0) = 1.07 - 1.15(1 - \mu_0) \quad (121)$$

In the above expressions W is the total cloud liquid water content, which is given as:

$$W = \int_{z_c}^{z_B} \rho(z) Q_c(z) dz \quad (122)$$

where

$\rho(z)$ = the air density,
z_B = the cloud top,
z_c = the cloud base.

The units of W are gm^{-2} and γ=0.021.

$$F_B = -F_B\downarrow\{1 - R(\mu_0)\} \quad (123)$$

where

$F_B\downarrow$ = the downward solar flux at the top of the cloud.

The derivation of cloud water mixing ratio Q_c is described in the appendix.

4.8.2 Longwave Radiation

The parameterization of longwave radiation relies on the values of external conditions: T_B and T_C are the absolute temperatures at the cloud top and the cloud base, respectively. $G_B\downarrow$ is the downward longwave flux at the cloud top. $G_C\uparrow$ is the upward longwave flux at the cloud base. The infrared flux profiles in the layered cloud are given as:

$$G(z) = G_L\exp[- (z - z_c)/\lambda_L] + G_U\exp[- (z_B - z)/\lambda_U] \quad (124)$$

where

$$G_L = \{ G_0 - G_1\exp[- (z_B - z_c)/\lambda_U]\}/D \quad (125)$$

$$G_U = \{ G_1 - G_0\exp[- (z_B - z_c)/\lambda_L]\}/D \quad (126)$$

$$D = 1 - \exp\{ - (z_B - z_c)/\lambda_N \} \quad (127)$$

$$\frac{1}{\lambda_N} = \frac{1}{\lambda_U} + \frac{1}{\lambda_L} \quad (128)$$

$$G_0 = G_C\uparrow - B_C + (B_C - G_B\downarrow)\exp(-\eta) \quad (129)$$

$$G_1 = (G_C\uparrow + B_B - 2B_C)\exp(-\eta\uparrow) + B_B - G_B\downarrow \quad (130)$$

$$\eta\uparrow,\downarrow = \alpha\uparrow,\downarrow W \quad (131)$$

$$\alpha\uparrow = 0.13 \text{ and } \alpha\downarrow = 0.158 \quad (132)$$

$$B_C = \sigma T_C^4 \quad (133)$$

$$B_B = \sigma T_B^4 \quad (134)$$

$$\lambda_L = 70W/(W - W^{1/2} + 2.67) \quad (135)$$

$$\lambda_U = 140W^{-0.56} \quad (136)$$

where

σ = the Stephan-Boltzmann constant.

4.9 Cloud Condensation

Conservation equations for the mixing ratios of water vapor and cloud water, and the potential temperature, are written as follows:

$$\frac{\partial Q_v}{\partial t} = -(Cond)_v \quad (137)$$

$$\frac{\partial Q_c}{\partial t} = (Cond)_v \tag{138}$$

$$\frac{\partial \Theta}{\partial t} = \frac{\Theta}{T}\frac{L_v}{C_p}(Cond)_v \tag{139}$$

where

Q_v Q_c = the mixing ratios of water vapor and cloud water.
Θ = potential temperature,
T = absolute temperature,
L_v = latent heat of condensation,
C_p = specific heat of dry air at constant pressure,

and

$(Cond)_v$ = the rate change of the mixing ratio due to condensation.

Define:

$$Q_w = Q_v + Q_c \tag{140}$$

$$\Theta_l = \Theta - \frac{\Theta L_v}{T c_p} Q_c \tag{141))}$$

where

Q_w = the total water

Θ_l = liquid water potential temperature. [25]

In model operation, Q_c is initially zero, and Q_v comes from initial input data. By adding equations (137) and (138), we obtain:

$$\frac{\partial Q_w}{\partial t}=0 \tag{142}$$

By subtracting equation (138) x $(\theta/T)(L_v/c_p)Q_c$ from equation (139), we obtain:

$$\frac{\partial \Theta_l}{\partial t}=0 \tag{143}$$

Thus, Q_w and θ_l conserve their quantity even when a phase change occurs.

In order to recover the potential (or absolute) temperature and the mixing ratios of water vapor (Q_v) and cloud liquid water (Q_c), the probabilty density function, G, proposed by Sommeria and Deardoff [26] and Mellor, [27] is used. The probability density function in assumed to be Gaussian such that:

$$G=\frac{1}{2\pi\sigma_{\theta l}\sigma_{qw}(1-r^2)^{1/2}}\exp\left[-\frac{1}{(1-r^2)}\left(\frac{\theta_l^2}{2\sigma_{\theta l}^2}-r\frac{\theta_l q_w}{\sigma_{\theta l}\sigma_{qw}}+\frac{q_w^2}{2\sigma_{qw}^2}\right)\right] \tag{144}$$

where

θ_l = fluctuation of liquid water potential temperature,
q_w = the fluctuation of total water mixing ratio,

and

$$\sigma_{\theta l}=\overline{\theta_l^2} \tag{145}$$

$$\sigma_{qw}{}^2=\overline{q_w{}^2} \tag{146}$$

$$r=\frac{\overline{\theta_l q_w}}{\sigma_{\theta l}\sigma_{qw}} \tag{147}$$

The local condensation is assumed to be given by:

$$Q_l = (Q_w - Q_s)H(Q_w - Q_s) \tag{148}$$

where

Q_s = saturation mixing ratio,
$H(x)$ = Heaviside function,

defined as:

$$H(x)= 0,\ x<0 \tag{149}$$

$$H(x)= 1,\ x>0$$

The following parameters are defined as:

$$a=(1+Q_{sl,T}\frac{L_v}{c_p})^{-1} \tag{150}$$

$$b=a\frac{<T>}{<\theta>}Q_{sl,T} \tag{151}$$

$$\Delta Q = Q_w - Q_{sl} \tag{152}$$

$$Q_{sl,T}=(\frac{\partial Q_s}{\partial T})_{T=T_l}=0.622\frac{L_v}{R_d}\frac{Q_{sl}}{T_l^2} \tag{153}$$

$$Q_{sl}= 0.622e_s(T_l)/(P - e_s(T_l)) \tag{154}$$

$$e_s(T)=6.11\exp[\frac{L_v}{R_d}(\frac{1}{273}-\frac{1}{T_l})] \tag{155}$$

and

$$T_l = (P/P_0)^k\Theta_l \tag{156}$$

where

Q_{sl} = mean saturation mixing ratio of water vapor at T_l;

Θ_l = liquid water potential temperature defined by equation (138);

$e_s(T_l)$ = saturation water vapor pressure at T_l;

and

R_w = the gas constant for water vapor.

A function R which indicates a fraction of cloud coverage for a given volume of air is given by Mellor: [27]

$$R=\int_{-\infty}^{\infty}\int_{-\infty}^{\infty}H(Q_w-Q_s)GdQ_w d\theta_l=\frac{1}{2}[1+erf(Q_1/2\sqrt{2})] \tag{157}$$

$$erf(x)=\frac{2}{\sqrt{\pi}}\int_0^x \exp(-y^2)dy \tag{158}$$

Cloud water mixing ratio Q_c is given by:

$$Q_c=2\sigma_s[RQ_1+\frac{1}{\sqrt{2\pi}}\exp(-\frac{Q_1^2}{2})] \tag{159}$$

where

$$Q_1=a\frac{\Delta Q}{2\sigma_s} \tag{160}$$

$$\sigma_s^2=\frac{1}{4}(a^2\overline{q_2^2}-2ab\overline{q_w\theta_l}+b^2\overline{\theta_l^2}) \tag{161}$$

Furthermore,

$$\overline{q_c\theta_l}/(a\overline{q_w\theta_l}-b\overline{\theta_l^2})=\overline{q_cq_w}/a\overline{q_w^2}-b\overline{q_w\theta_l}=R' \tag{162}$$

and

$$\overline{u_jq_c}/a\overline{u_jq_w}-b\overline{u_j\theta_l}=R' \tag{163}$$

where

$$R'=R-\frac{Q_1}{2\sigma_s}\frac{1}{\sqrt{2\pi}}\exp[-\frac{Q_1^2}{2}]. \tag{164}$$

However, due apparently in part to coarse vertical grid spacing, and the nudging discussed later in section 5.2 the values of σ_s calculated by equation (161) are typically too low. In the current BFM, a constant value of 0.000275 is used instead. This was found to be typical of partly cloudy skies by Sommeria and Deardoff. [26] If model nudging is turned off, equation (161) seems to yield more realistic values. Finally, q_c^2, the variance of the cloud water mixing ratio, is expressed as:

$$\frac{\overline{q_c^2}}{4\sigma_s^2}=R[1+(Q_1-2\frac{Q_c}{2\sigma_s})]+(Q_1-\frac{Q_c}{2\sigma_s})\frac{1}{\sqrt{2\pi}}\exp[-\frac{Q_1^2}{2}]. \tag{165}$$

Figure 7 shows R, $Q_c/2\sigma_s$, and $q_c^2/4\sigma_s^2$ as a function of Q_1 obtained according to equations (157), (159), and (165), respectively. As seen from Figure 7, a fraction of cloud coverage R varies gradually with Q_1 and takes non-zero values even if Q_1 is negative. In other words, clouds can exist even if the mixing ratio of water vapor averaged over a grid volume is not saturated. This is realistic because the grid spacing normally used in mesoscale models is larger than the size of small clouds. Therefore, the present cloud model can use a relatively large grid spacing that could save computational time substantially. A statistical cloud model such as the present one avoids the ambiguous condensation criteria often used by coarse grid models in which saturation values are lowered arbitrarily to compensate for the amount of cloud that is not resolved by the grid.

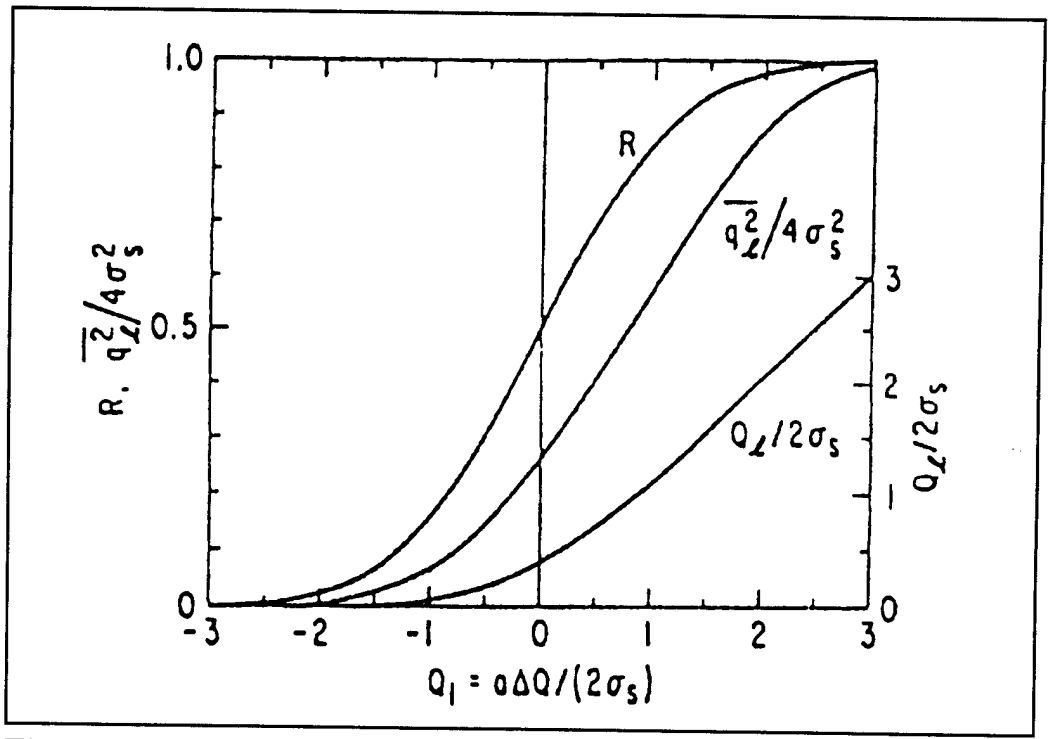

Figure 7. Relationships showing R, $Q_1/2\sigma_s$, and $q_c^2/4\sigma_s^2$ as a function of Q_1 (= a (Q_W-Q_{sl}) $/2\sigma_s$).

In the BFM, the total cloud water content (W) from the ground surface to the top of the model atmosphere is calculated and the horizontal distribution of W is displayed. W is calculated as:

$$W=\int_{z_g}^{H}\rho_a Q_c dz=\frac{\overline{H}+z_{gmax}-z_g}{\overline{H}}\int_0^{\overline{H}}\rho_a Q_c dz \quad * \tag{166}$$

where

ρ = air density,

z_{gmax} = highest terrain elevation value in the BFM 51 by 51 model domain.

4.10 Non-Convective Precipitation Rate

Because microphysical processes of non-convective precipitation formation are not included in the model, the non-convective precipitation rate is parameterized as a function of cloud liquid water. The scheme developed by Sundqvist *et al.* for non-convective precipitation rate is incorporated into the BFM. [28] The basic assumption is that the denser the cloud, the higher the precipitation rate.

The rate of release of non-convective precipitation is described by

$$P=C_0 Q_c[1-\exp(-(\frac{Q_c}{RQ_{c,cr}})^2] \tag{167}$$

where

$1/C_0$ = characteristic time for the conversion of cloud droplets into precipitation particles (raindrops, or snow particles),

R = fraction of cloud coverage described in the previous section,

$Q_{c,cr}$ = threshold value for cloud water, which Q_c/R must exceed before the release of precipitation can become efficient.

The parameter $Q_{c,cr}$ should have a value typical of individual cloud type, which is invariant to grid resolution.

The rate of non-convective precipitation, $P_r(z^*)$, at a z^*-level is given by

$$P_r(z^{**}) = \int_0^H \rho P dz = \left(\frac{\overline{H} + z_{gmax} - z_g}{\overline{H}}\right) \int_{z^*}^{\overline{H}} \rho(z^*) P dz^* \qquad (168)$$

where

H = depth of the model atmosphere,

z_{gmax} = highest terrain elevation in the BFM model 51 by 51 domain,

z_g = terrain elevation, and ρ is the air density.

To simulate the coalescence process, Sundqvist *et al.* introduced an additional parameter F_∞. [28] This parameter increases with the rate of precipitation and multiplies C_0 and divides $Q_{c,cr}$. The relation is:

$$F_\infty(z^*) = 1 + C_1 Pr(z^*)^{1/2} \quad . \qquad (169)$$

Similarly, C_0 increases and $Q_{c,cr}$ decreases by a temperature function F_{BF} when the temperature is lower than -5 °C in clouds containing a mixture of droplets and ice crystals (Bergeron-Findeisen mechanism). This formulation is:

$$F_{BF}= 1 + C_2(268.0 - T(z^*))^{1/2} . \quad (170)$$

The two modified parameters C_{0F} and $Q_{(c,cr)F}$ become, respectively:

$$C_{0F} = C_0 \circ F_\infty \circ F_{BF} \quad (171)$$

and

$$Q_{(c,cr)F}=Q_{c,cr}/(F_\infty \cdot F_{BF}) . \quad (172)$$

The effects of evaporation as precipitation falls through subsaturated layers is not included. Also, the non-convective precipitation rate at the surface is calculated as:

$$P_r(0)=\left(\frac{\overline{H}+z_{gmax}-z_g}{\overline{H}}\right)\frac{1}{\rho_w}\int_0^{\overline{H}}\rho(z^*)C_{0F}Q_c(z^*)\left[1-\exp\left(-\left(\frac{Q_c(z^*)}{RQ_{(c,cr)F}}\right)^{1/2}\right)\right]dz^* \quad (173)$$

where

ρ_w = density of water.

$P_r(0)$ is calculated in the unit of (mm/h) or (in/h).

4.11 Sea Surface Temperature and Soil Characteristics

4.11.1 Sea Surface Temperature

In the BFM, water temperature stays independent of diurnal change of the solar angle, but the monthly average global sea surface temperature distribution data, obtained from the U.S. Air Force Combat Climatology Center, is used to give the temperatures of sea water. The data is given at about every 0.5°. The temperatures of the grids over sea surface in the model domain are given by those adjacent in the data set. Currently, water temperatures of inland water bodies such as the Great Lakes and the Salt Lake must be given by changing the source program before application of the model.

4.11.2 Surface Characteristics

Ground surface albedo and emissivity, specific heat, density, and heat conductivity of soil are given as a function of the month of year, and latitudes of the model grids. The values of these parameters are roughly estimated from the book by Pielke. [28]

For snow cases, the user can specify that snow can be assumed over the entire grids above a particular altitude by manually setting flags in the file snow.d. For the land grid points that are snow covered, albedos, emissivities and soil heat conductivities are internally hardcoded to those typical of snow, and soil temperature is fixed at - 1 °C. This has not yet been added as part of the IMETS BFM execution GUI, so for now this file is set to "no snow."

5. Initialization and Assimilation of Data

5.1 Initialization

Initialization of the BFM is done as follows. The initial wind field over the entire model domain is given uniformly by the average wind vector field calculated by the mean wind direction at the tenth layer (Z^*= 1,195 m), and the maximum wind speed of the following two:

Mean wind speed at the tenth layer, and
$(0.4/k)\log([z^* + 0.1\}/0.1)$

where

k = Karman constant.

The average wind direction and speed at the tenth layer are calculated from the three-dimensional data obtained from the analysis of the GSM, and upper air sounding data. Initial fields of potential temperature and water vapor mixing ratio are also obtained from the same data.

Suppose a forecast calculation is initialized at time T_0. Pre-calculation will start at time T_0-3 h, and for 3 h from T_0 - 3 to T_0 the model fields are dynamically adjusted to the initial fields by the nudging method which is described in the following sections. During the 3-h initialization period, surface data observed at the time T_0 is also nudged to the model fields. The nudging method of surface data will be described later.

When the GSM forecast data for time T_0, T_0 + 12, and T_0 + 24 h are available, the hourly lateral boundary condition data between T_0 and T_0 + 12, and/or T_0 + 12 and T_0 + 24 are calculated by a linear interpolation method. At time T_0, the data for T_0

+ 1 are assimilated in for 1 h, and this process is repeated for an entire forecast period.

When only upper air sounding and surface data are available, initialization is done in a similar manner as when the GSM data is available, but after the time T_0, the magnitudes of nudging parameters C_n are reduced gradually as exp(-a·t), where t is the forecast duration after T_0, and a is a coefficient determined empirically. The forecast period is limited to 6 h.

5.2 Nudging Method

To assimilate temporal and spatial changes of synoptic flows, which are obtained from the GSM and upper air sounding data, nudging terms are added to the model equations (35), (36), (45), and (46) at all grid points, although the model can be run with nudging only at the lateral boundaries as well. By adding the nudging terms, the equations of horizontal wind vector components are modified as:

$$\frac{\partial U}{\partial t}=F_1+C_n(U_t-U) \tag{174}$$

$$\frac{\partial V}{\partial t}=F_2+C_n(V_t-V) \tag{175}$$

where

C_n = nudging coefficient,
U_t and V_t = target wind components of (respectively) x- and y- directions.

Target winds are described in the next section. F_1 and F_2 are the right-hand side terms of equations (35) and (36), respectively. The equations of potential temperature deviation and mixing ratio are written with nudging terms as follows:

$$\frac{\partial \delta\Theta_v}{\partial t} = F_3 + C_n(\delta\Theta_{v,obs} - \delta\Theta_v) \tag{176}$$

$$\frac{\partial Q_w}{\partial t} = F_4 + C_n(Q_{v,obs} - Q_w) \tag{177}$$

where

$\delta\Theta_v$ = deviation of virtual potential temperature from the base state virtual potential temperature,

$<\Theta_v>$ = defined earlier,

Q_v = water vapor mixing ratio,

obs = observed values, which are obtained from three-dimensional analysis of the GSM and upper air sounding data,

F_3 = right-hand side terms of equation (45),

F_4 = right-hand side of (46).

Recall that in the BFM, $<\theta_v>$ is the initially analyzed three-dimensional virtual potential temperature field, rather than the initial horizontally averaged values used by modelers such as Yamada. [5]

In the current version of the BFM, the nudging are enforced to the vertical layers above $z^* = 150$ m for potential temperature and moisture, and above $z^* = 14$ m for wind components. These are determined based on our long term experiences with nudging. The value of the nudging coefficient is set to 0.0003/s, roughly the

magnitude of the coriolis force. This is a value that has typically been used by many modelers such as Pielke, Yamada, and Zack *et al.* [29], [4], [30] This value seems to properly assimilate the large scale perturbations from the GSM, while at the same time allows the surface physics of the mesoscale model to have significant influence within the boundary layer, particularly near the surface.

5.3 Target Winds

Comparisons in the simulated wind fields, found by nudging to target wind components U_t and V_t ,and by nudging to the observed wind components U_{obs} and V_{obs} were conducted. [31] It showed that nudging to the target wind components produces better agreement between simulated and observed upper winds than nudging to the observed wind components.

Target wind components U_t and V_t are derived as follows. The equations of motion for horizontal wind vector components with the target winds under no frictional force can be written as:

$$\frac{\partial U}{\partial t}=f(V-V_g)+C_n(U_t-U) \tag{178}$$

$$\frac{\partial V}{\partial t}=-f(U-U_g)+C_n(V_t-V) \tag{179}$$

The solutions to the above equations at equilibrium ($t \to \infty$) are given by the following:

$$U=\frac{fC_n(V_t-V_g)+f^2U_g+C_n^2U_t}{C_n^2+f^2} \tag{180}$$

$$V=\frac{-fC_n(U_t-U_g)+f^2V_g+C_n^2V_t}{C_n^2+f^2} \tag{181}$$

Letting U and V approach U_{obs} and V_{obs} (respectively) and solving for U_t and V_t, the following equations are obtained:

$$U_t=U_{obs}-\frac{f}{C_n}(V_{obs}-V_g) \tag{182}$$

$$V_t=V_{obs}+\frac{f}{cm}(V_{obs}-V_g) \tag{183}$$

where

U_{obs} = the observed wind components in the x- direction

V_{obs} = the observed wind components in the y- direction

and

U_g = geostrophic wind components in the x- direction

V_g = geostrophic wind components in the y- directions.

U_t and V_t are generally different from the corresponding large-scale wind components. Observed winds might be used as target winds if the Coriolis force were absent, or if the observed winds are identical to the geostrophic winds. If only the observed winds are used in the nudging in all other cases, the solutions will generally be different from the observations.

The physical meaning of the target winds is that the solutions of the equations of motion, with the target winds, become identical to the observed winds in the absence of frictional effects. Thus, modeled winds should converge to observations in the layers far above the boundary layer where frictional effects are negligible. On the other hand, atmospheric turbulence in the boundary layer is significant because of frictional effects. The nudging terms play relatively minor roles. In summary, the nudging terms enforce the model winds to match observations in the free atmosphere, but they play a relatively minor role in the boundary layer.

5.4 Surface Data Nudging

Individual surface data within the model domain observed at initialization time T_0 is assimilated into model calculation at the grid points adjacent to the surface observation.

The third and forth layer data (z^*= 6 and 10 m, respectively) of the three-dimensional data for initialization calculated from the GSM and/or upper air sounding data at time T_0 are modified as follows:

$$\psi_{new}(i,j)=\psi(i,j)+\sum_{l=1}^{N}\frac{\psi_l}{r_l^2}/\sum_{l=1}^{N}\frac{1}{r_l^2} \qquad (184)$$

where

ψ_{new} = new values of a parameter ψ,
ψ_l = ψ at a surface station l.

r_l = distance from l to a grid point (i, j).

In order to limit spatially the influences of surface data, the nudging parameter at a grid point (i, j) is calculated as:

$$C_{n,new}(i,j) = C_n(i,j) + \sum_{l=1}^{N} C_l\left(1 - \frac{r_l^2}{R^2}\right) \qquad \text{for } r_l < R \quad (185)$$

and

$$C_{n,new}(i,j) = 0.0 \qquad \text{for } r_l \geq R \quad (186)$$

where

C_l = empirical parameter (0.1).

The critical distance R is 40 km for wind and 20 km for potential temperature deviation and water vapor mixing ratio. These values are determined empirically. The nudging parameter C_l is about three orders of magnitude greater than C_n to emphasize the effects on the model fields of surface data.

Surface data nudging is done for 3 h from T_0 - 3 to T_0. After T_0, instead of a sudden assignment of zero values to C_n, the influences of surface data are gradually decreased by multiplying exp(-kt) to C_n. Here k is an empirical coefficient, and t is the time after T_0.

6. Initialization Data and Some Examples of the BFM

In this section, the qualities of the GSM forecast data used as the BFM lateral boundary conditions, the initialization data produced by the three-dimensional analysis, and some examples of the BFM output are shown. Preliminary studies that attempt to make a statistical evaluation of the BFM output have been done by Henmi *et al.* [32] and Knapp and Dumais. [33] Henmi *et al.* studied the performance of the BFM using meteorological data observed at White Sands Missile Range (WSMR), NM, and showed that incorporation of surface data into the initial fields seems to produce more accurate BFM forecast results. Knapp and Dumais made comparison studies of observed data including upper air and surface data with the BFM, and the GSM output over a 250 x 250 km, and a 500 x 500 km area centered at Colorado Springs, CO. Statistical parameters such as the correlation coefficients and mean absolute residuals between observed data and model output data are calculated for horizontal wind vector components, temperature, and dew-point temperature. Knapp and Dumais concluded that the BFM forecasts of wind, temperature and dew points at the surface (and to a lesser degree with height above the surface) are significantly better than those by the GSM forecasts being used as the BFM lateral boundary conditions, particularly over complex terrain. As to the effects of grid spacing of the BFM, they did not find any significant improvement by adapting the 2.5 or 5 km grid spacing in place of the 10 km. It might be expected that these results could change when a convective parameterization scheme is incorporated. This problem will be further studied in the future. Currently, extensive studies using the data archived over different geographical and climatological regions (Bosnia, Korea, Florida, southern California, and the northeast U.S.) during different seasons of the year are under way and the results will be presented in the future.

6.1 Qualities of the GSM Forecast Data

Initialization and time-dependent boundary condition data for the BFM are provided by the GSM forecast data. Because the GSM analysis and forecast data are delivered about 6 to 7 h after the forecast base time, the GSM analysis data fields are not used for operational initialization of the BFM forecast calculations; the 12, 24, 36 and 48-h GSM forecast data fields are used. For example, to initialize a BFM forecast at 12 GMT, the 12 GMT upper air radiosonde and surface sensor data, along with the GSM gridded 12-h forecast fields from the previous 00 GMT initialized run are used. Time-dependent boundary values for the 12 GMT run come from the GSM 00 GMT base time 24, 36 and 48-h gridded forecast fields.

In this section, the 12 and 24-h forecast data generated by the GSM have been spatially interpolated to the radiosonde sounding site locations, and compared with the observation. The GSM data calculated at different pressure levels (200, 300, 500, 700, and 850 mb) are compared with the corresponding observed data. The data at 1000 mb are excluded due to the lack of sounding data at this level for the stations in the areas selected for study. The data are obtained from the 1,600 x 1,600 km areas centered at the following geographical areas and dates/hours as shown in table 2.

Table 2. Locations, dates, and hours of upper air sounding data used for comparison with GSM data

Location	Longitude	Latitude	Base Time+ Dates/Hour
Tuzla, Bosina	18.657 E	44.470 N	12/13/12Z,12/14/00 Z12/14/12Z,12/15/0 0Z 12/19/12Z,12/20/00 Z 12/20/12Z,12/21/00 Z 12/21/12Z
Denver, CO	104.717W	38.17N	7/24/12Z,7/31/12Z 8/1/00Z,8/1/12Z 8/2/00Z, 8/7/12Z 8/8/00Z
Ft. Irwin, CA	116.066W	34.257 N	1/4/12Z,1/5/00Z 1/10/12Z,1/11/00Z 1/23/00Z,1/24/12Z 1/25/00Z, 1/31/12Z

In table 2, 12/13/12Z means that the GSM base time is 13 December, 12 GMT. The data is taken during the periods of July 1995 through January 1996.

The correlation coefficients r, and linear relationships $y = A + Bx$ between the GSM data (y) and the upper air sounding data (x) at different pressure levels, and those of the entire data set are calculated for the 12 and 24- hour forecast data.

The results are given in table 3. Scatter diagrams showing the relationships between the GSM data and upper air sounding data for the entire data sets are shown in figure 8A through 8D.

Table 3. Correlation coefficients between the GSM data and upper air data

Pressure levels (mb)	Temperature		Dew pt. Temp.		x_comp. of wind, u		y-comp. of wind, v	
	12 h	24 h	12 h	24 h	12 h	24 h	12 h	24 h
850	r=.83	r=.85	r=.66	r=.59	r=.48	r=.52	r=.28	r=.38
	A=.71	A=.58	A=.71	A=-.28	A=.23	A=1.03	A=-.36	A=-1.97
	B=.86	B=.84	B=.71	B=.63	B=.58	B=.65	B=.28	B=.40
700	r=.78	r=.82	r=.60	r=.54	r=.56	r=.64	r=.34	r=.56
	A=-1.5	A=-1.2	A=-4.0	A=-5.6	A=1.2	A=1.7	A=-1.2	A=-1.6
	B=.86	B=.86	B=.59	B=.59	B=.65	B=.75	B=.36	B=.65
500	r=.65	r=.71	r=.63	r=.51	r=.63	r=.76	r=.55	r=.59
	A=-7.8	A=-14.2	A=-11.1	A=-14.	A=2.3	A=2.3	A=-1.2	A=-1.6
	B=.62	B=.55	B=.59	B=.46	B=.7	B=.8	B=.58	B=.64
300	r=.94	r=.95	r=.59	r=.59	r=.72	r=.72	r=.66	r=.67
	A=-5.8	A=-6.2	A=-23.	A=-25.	A=3.6	A=5.5	A=-2.3	A=-3.4
	B=.85	B=.81	B=.52	B=.48	B=.72	B=.73	B=.71	B.64
200	r=.72	r=.81			r=.73	r=.75	r=.67	r=.77
	A=-21.	A=-20.			A=3.8	A=3.5	A=3.8	A=3.5
	B=.60	B=.81			B=.77	B=.86	B=.83	B=.73
Entire Data	r=.97	r=.97	r=.89	r=.87	r=.70	r=.76	r=.58	r=.66
	A=-2.3	A=-1.8	A=-2.6	A=-3.9	A=1.7	A=2.4	A=-1.8	A=-2.4
	B=.94	B=.93	B=1.0	B=.94	B=.77	B=.83	B=.64	B=.67

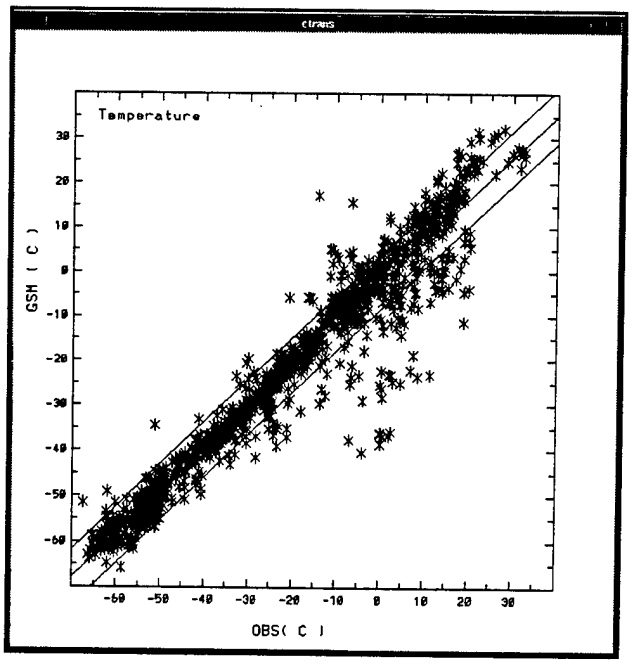

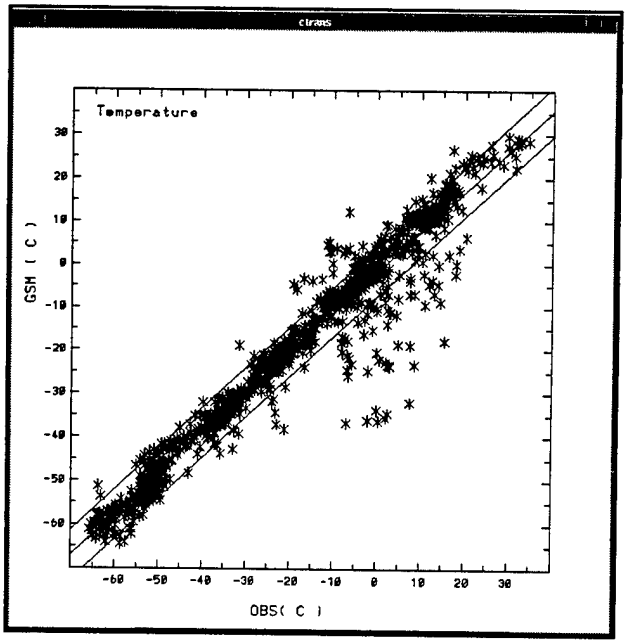

Figure 8A. Relationship between the GSM (top) for 12-h forecasting data and upper air sounding data for temperature for the 24-h forecast data (bottom).

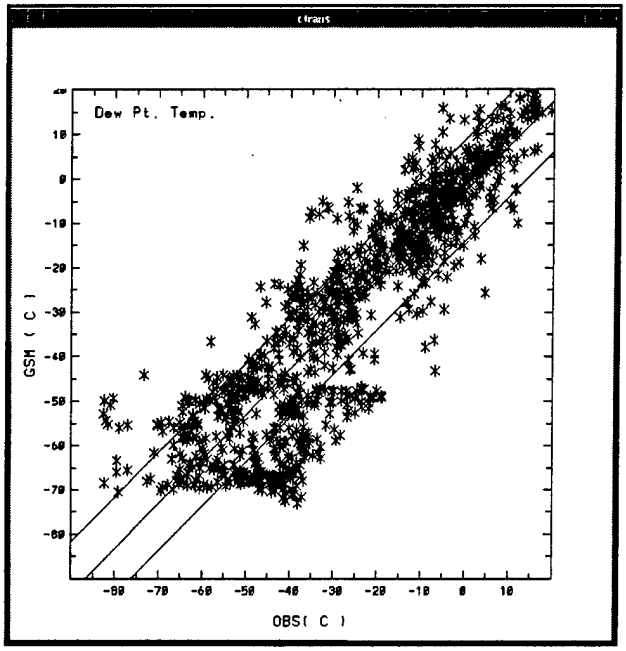

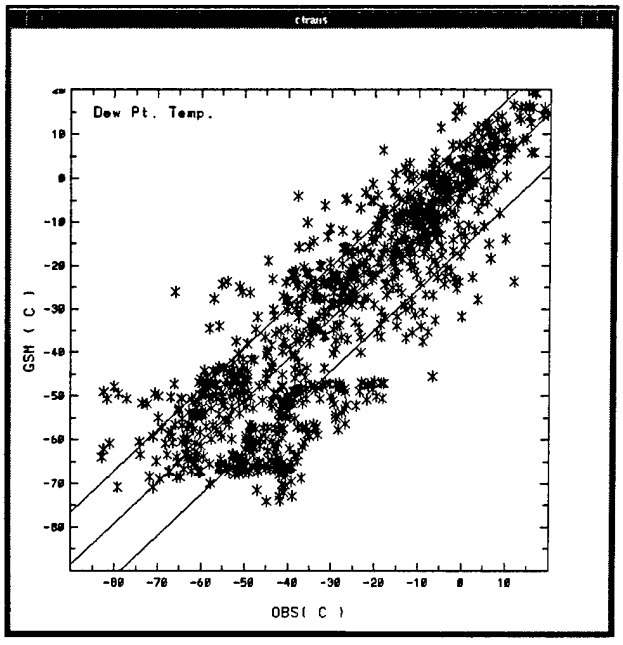

Figure 8B. Same as figure 8A, except for dew point temperature.

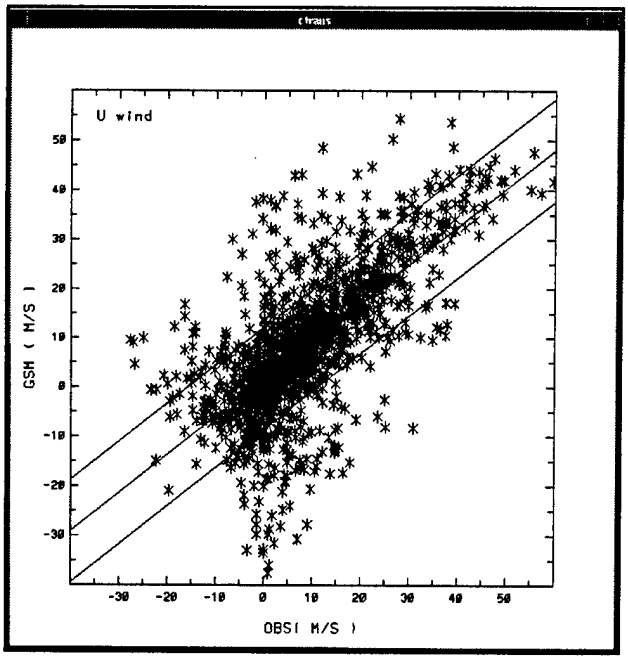

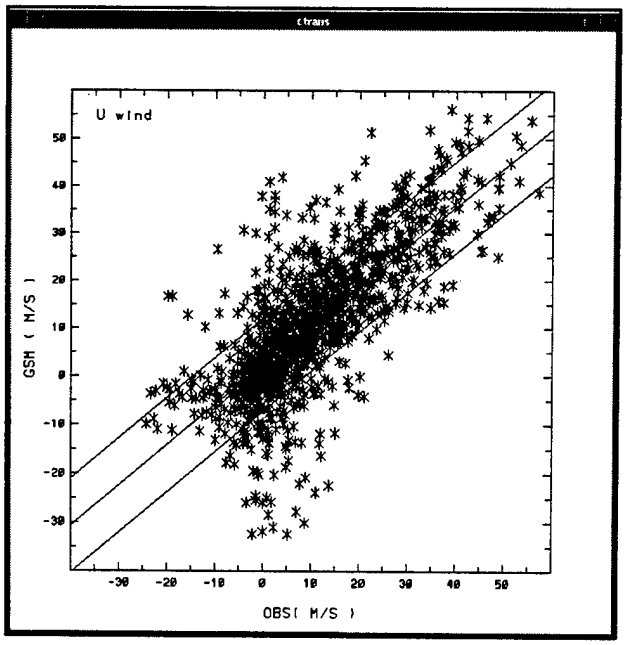

Figure 8C. Same as figure 8A, except for east-west components of horizontal wind vectors.

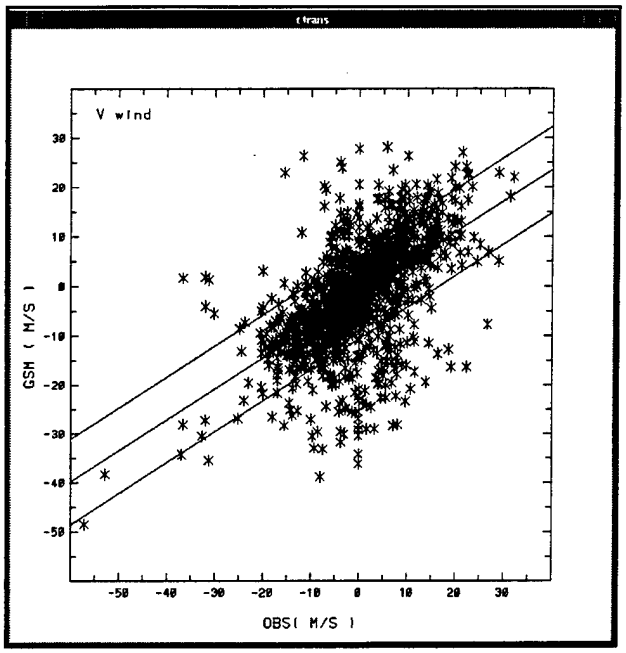

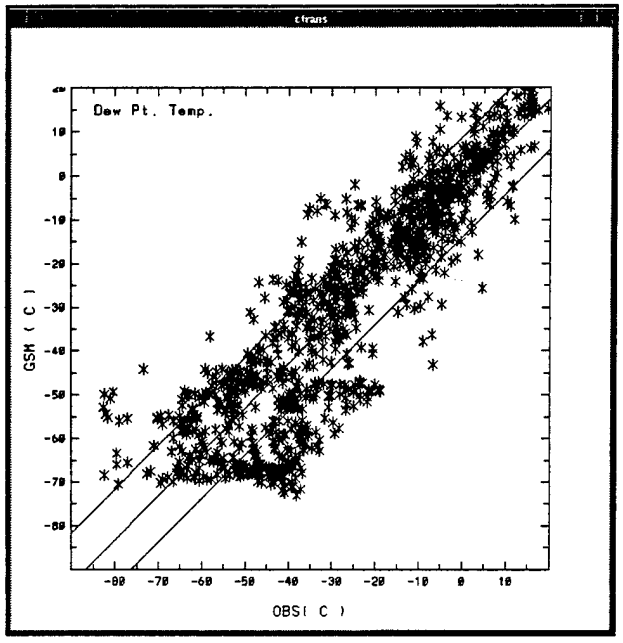

Figure 8D. Same as figure 8A, except for north-south components of horizontal wind vectors.

From the table and figures, the following can be inferred:

- Among the four parameters, temperature shows the best agreement between the GSM and the sounding data. Dew point temperature and wind components (particularly the north-south wind component) show considerable dispersion.

- For both temperature and dew point temperature, the GSM forecast data tends to show lower values than observed at higher pressure levels. See the values of A at 500, 300 and 200-mb levels. Restated, the GSM atmosphere is drier than the observed atmosphere in the upper levels.

- For the wind components, the GSM tends to underforecast wind speeds in larger wind speed cases (such as jet streams).

- The GSM forecasting skills for 12 and 24 h do not show significant differences.

- When the GSM forecast data is used as the initial and boundary condition data for the BFM, it should be improved as much as possible, particularly for dew point temperature, horizontal wind components.

The U.S. Air Force Air Weather Service publication cites the following shortcomings of the GSM forecast, as the findings of the the U.S. Air Force Global Weather Central: [34]

- Long waves are not handled well because the model was designed for flight-level forecasting.
- Forecast wind speeds are typically too slow below the 100 mb level.
- Moisture forecasts are typically too dry.

- The model is generally too warm in the troposphere.
- Geopotential heights are generally too high.

From the list, 2 and 3 are in agreement with our findings; however, 4 does not agree, which shows the GSM temperature as slightly cooler than observation in the lower levels and slightly warmer in higher levels. We cannot compare 1 and 5 because no study has been done. Our experience has also shown that the GSM analysis fields tend to produce interpolated grid point surface level wind speeds that are too high, and surface level temperatures that are either too low (during afternoons) or too high (during late night/early morning). A more detailed study using the data of many different days and areas is necessary.

6.2 Initialization Fields for the BFM Forecasting Calculation

As mentioned previously, the BFM forecast model is initialized by nudging the BFM field for 3 h from T_0 -3 to T_0 to the three-dimensional fields produced by the objective analysis, where T_0 is the forecast base time. The three-dimensional fields are created by compositing the GSM data and upper air sounding data (composited data) when both are available. Furthermore, when surface observation data is available, the third and fourth layers of the BFM data are modified by nudging to the surface data for 3 h from T_0 - 3 to T_0. In the following, the differences of the initialization data produced by the above methods are shown, using the data over the Bosnia area at 12 GMT, 24 Aug 96.

Figure 9 shows a horizontal wind vector distribution at 10 m AGL, produced by compositing the GSM 00 GMT base time 12-h forecast field with the available upper-air sounding data at 12 GMT, 24 Aug 95. Wind directions are predominantly from the west. Figure 10 shows observed horizontal wind vectors at the same level and at the same time. Observed wind directions at the surface

were southerly. The BFM fields are nudged toward these fields for 3 h from T_0 - 3 (9 GMT) to T_0 (12 GMT).

Figure 11 (top) is the stream line distribution at the 10 m level obtained by nudging for 3 h to both fields (the composited data and the surface observation data). For comparison, figure 11 (bottom) is the streamline obtained by nudging to only the composited data. Nudging to the surface observation data has produced significantly different fields for initialization.

Figure 12 (top) and (bottom) are the surface temperature distributions at the same time. The top figure is the result by nudging to both the composited data and the surface observed data, and (bottom) is the result obtained by nudging only to the composited data. For this case, there are not significant differences in the surface temperature distribution between the composited data and the observation. The distribution patterns are fairly similar between the two figures.

Figure 13 (top) and (bottom) are the dew point temperature distributions at the 10-m level. The top figure was produced by nudging to both the composited data and the surface observed data, and the bottom figure by nudging to only the composited data. There are significant differences between the two figures. Figure 13 (top) shows localized distributions of dew point temperature created by the strongly localized nudging parameter.

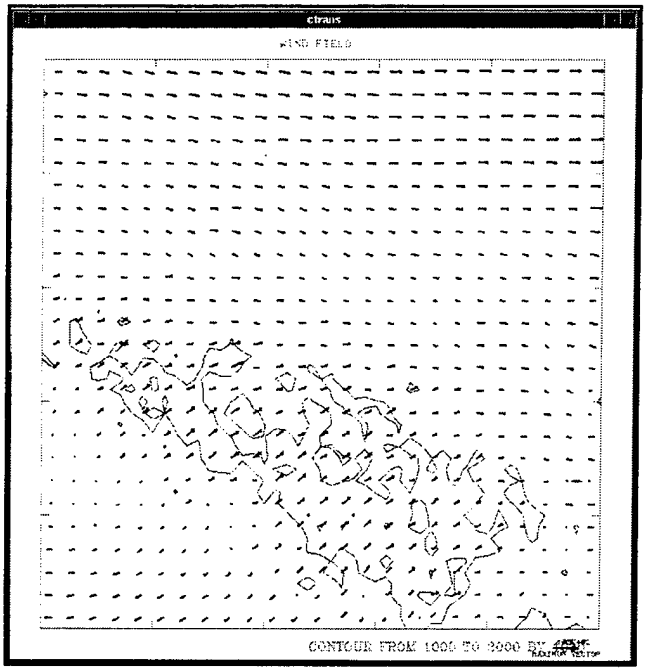

Figure 9. Horizontal wind vector distribution at 10 m AGL, produced by compositing the GSM and upper air sounding data for 12 GMT, 24 Aug 95, over Bosnia.

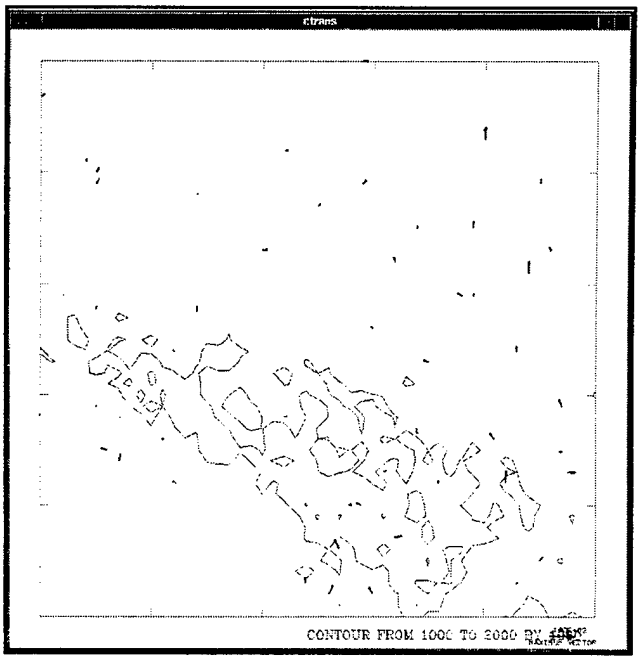

Figure 10. Surface wind vectors observed at 12 GMT, 24 Aug 96, over Bosnia.

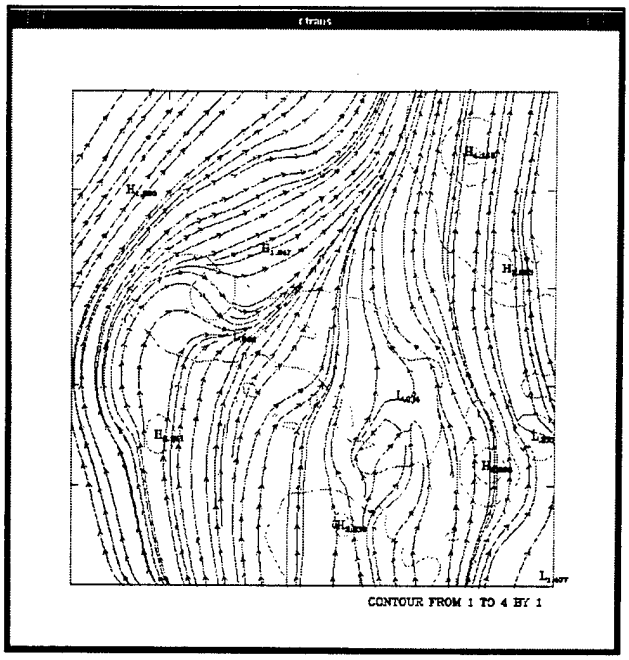

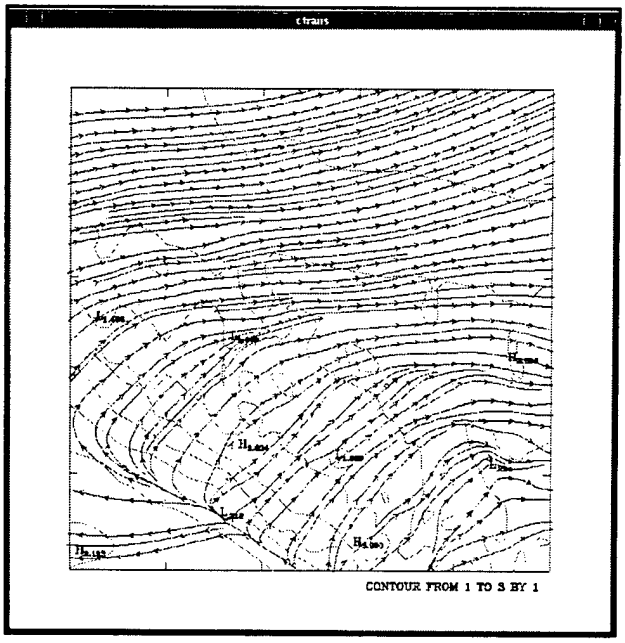

Figure 11. Streamlines and isotachs at the 10-m level, at time T_0 = 0 h for surface wind data nudged (top), and for surface wind data not nudged (bottom).

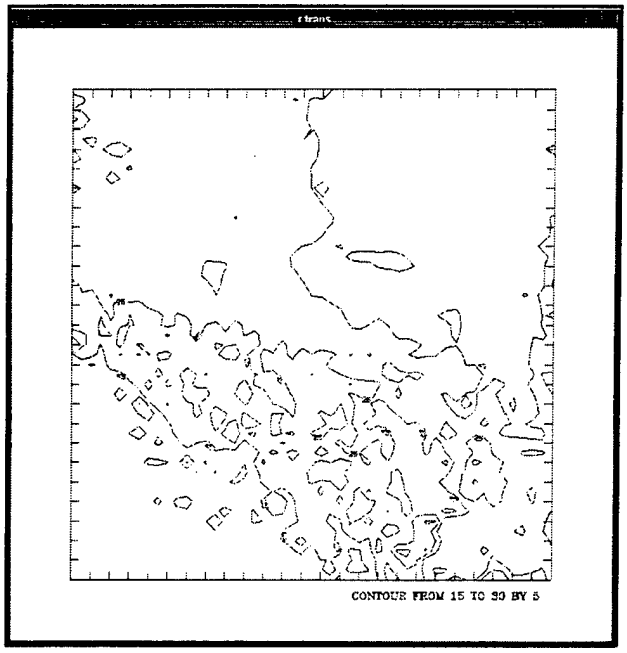

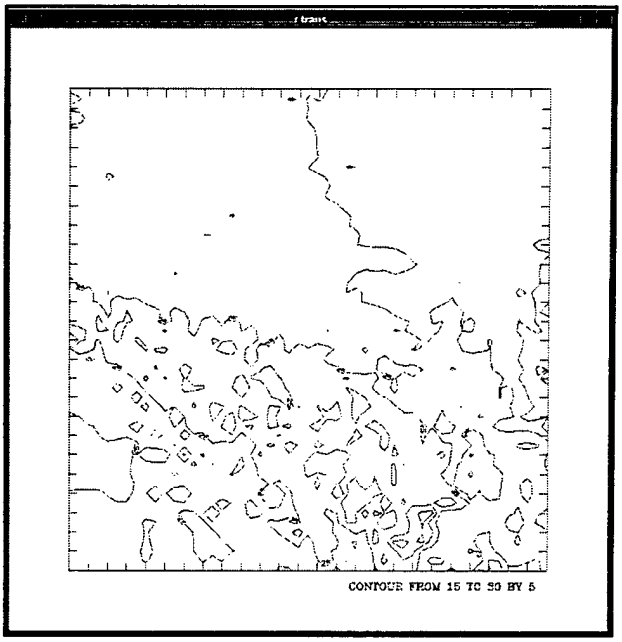

Figure 12. Temperature distribution at the 10 m level, at T_0 = 0 h for surface data nudged (top), and for not nudged (bottom).

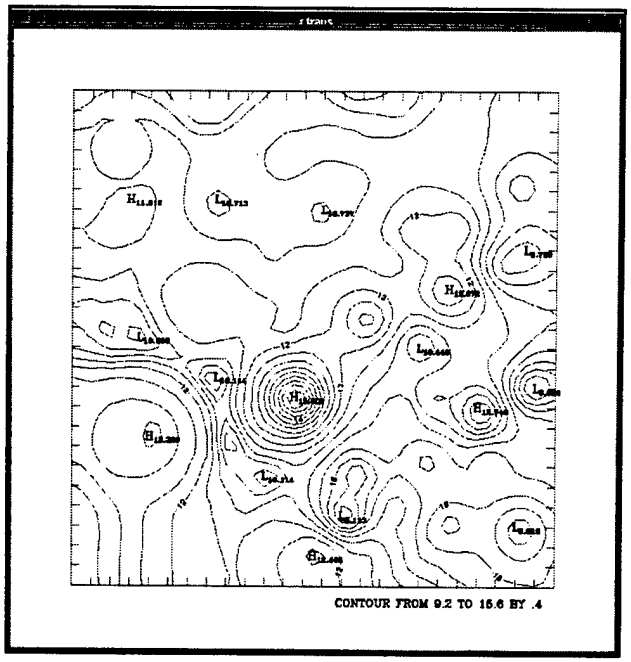

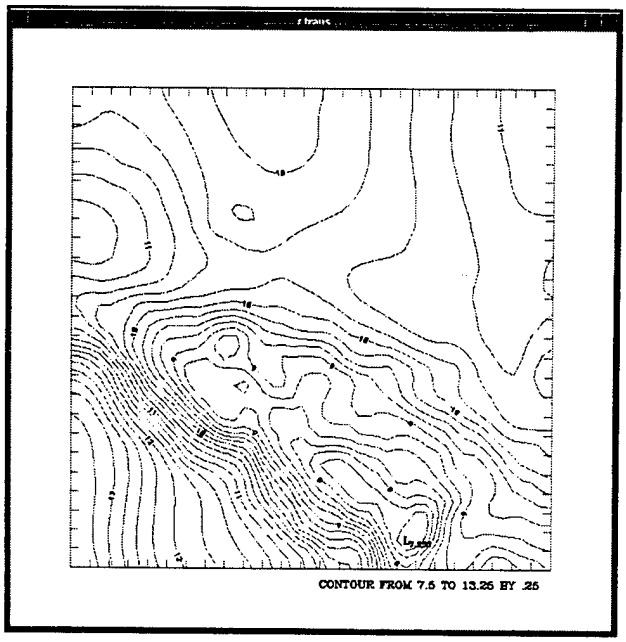

Figure 13. Dew point temperature distribution at the 10-m level at T_0 = 0 h (top) for surface wind data nudged, and for not nudged (bottom).

6.3 The Effects of Initial Data Fields on BFM Output at the Surface

The previous section showed that the initialization fields, produced by nudging to both the composited data and the surface observation data, were significantly different from those produced by nudging to only the composited data. To examine how the initial fields of the surface layers influence the BFM forecast fields, the BFM forecast calculations are made using the two different initial fields. Where surface nudging is used, the magnitude of the nudging is damped in time by a factor of exp(-kt), where k is an empirical coefficient and t is the time after T_0.

Figure 14 (top and bottom) are the streamline and isotach distributions at 10 m AGL at $T_0 = 3$ h. Figure 14 (top) is the result obtained using both composited and surface observation data, and (bottom) is the result obtained by using only the composited data. There are significant differences between the two images, which show the influences of the initial data (figure 11). However, at $T_0 = 6$ h (figure 15, top and bottom) the two become similar to each other. The influences of different initial surface data almost disappear, and the lateral boundary condition and the model's boundary layer physics take control of the surface layer wind flow patterns.

Figures 16 and 17 show the surface temperature (2 m AGL) distributions at forecast time $T_0 = 3$ h and $T_0 = 6$ h, respectively. Figures 18 and 19 are the surface dew point temperature distributions at $T_0 = 3$ h and $T_0 = 6$ h, respectively. In these figures, the top is the result generated by the composited and the surface observation data, and the bottom is the result generated by the composited data only. Similar to wind streamline distributions, at $T_0 = 3$ h, the influences of initial data can be detected, but at $T_0 = 6$ h, the patterns of the top and bottom images in figures 17 and 19 become very similar.

It may be concluded that after several hours of forecast calculation the influences of surface data disappear in the BFM output fields, and that the model physics and the lateral boundary conditions become dominant to the BFM's fields of surface wind, temperature, and dew point temperature.

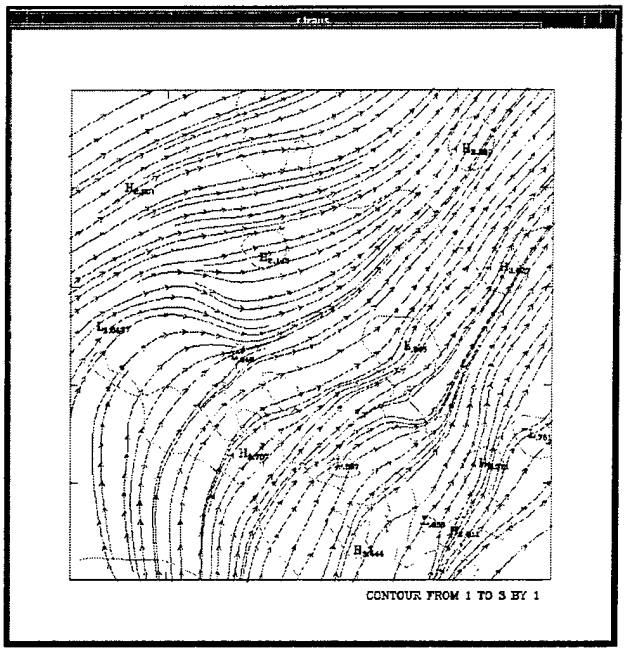

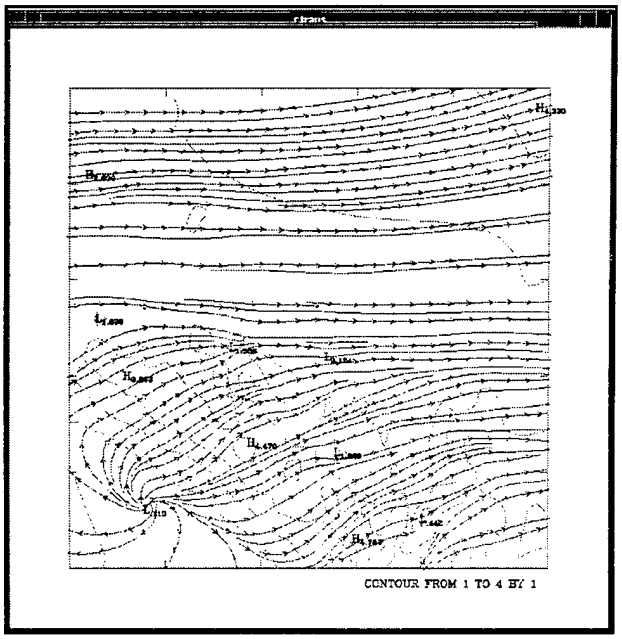

Figure 14. Same as figure 11, except for $T_0 = 3$ h.

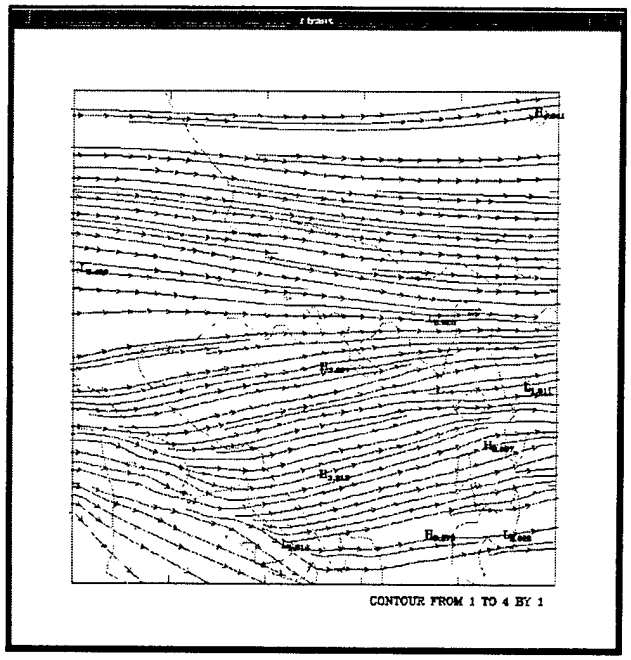

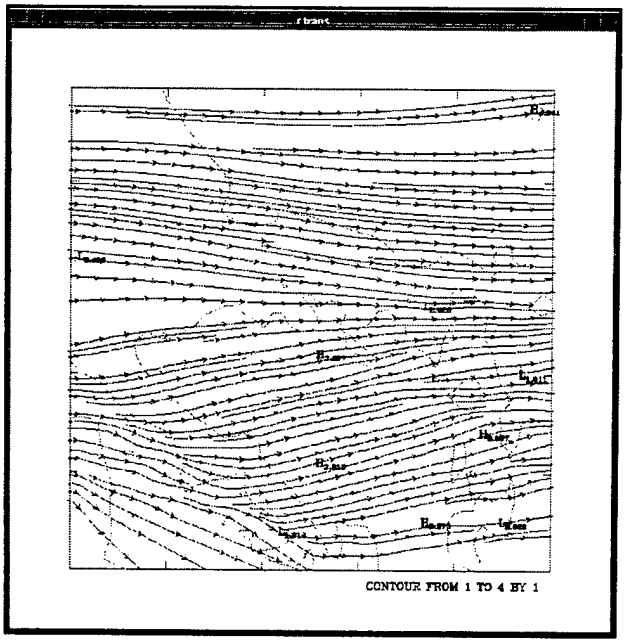

Figure 15. Same as figure 11, except for T_0 = 6 h.

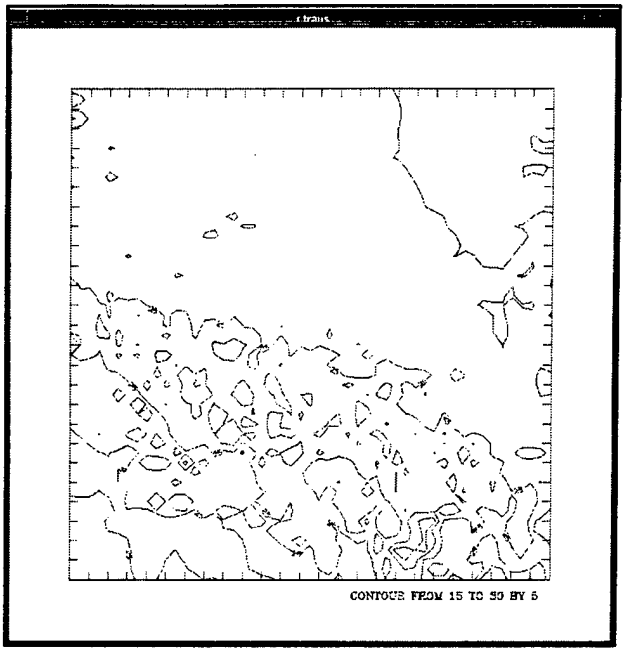

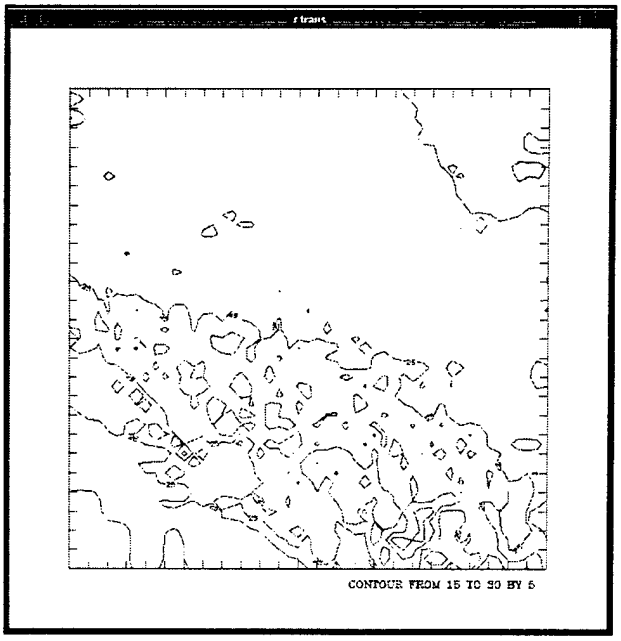

Figure 16. Same as figure 12, except for $T_0 = 3$ h.

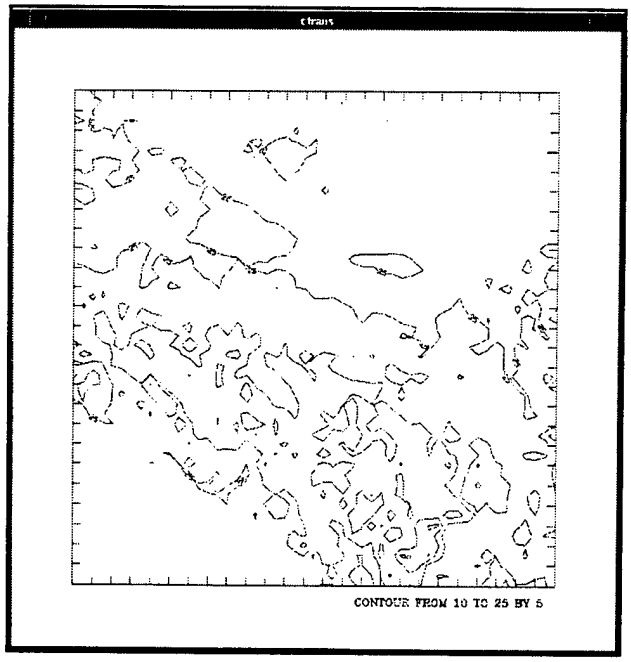

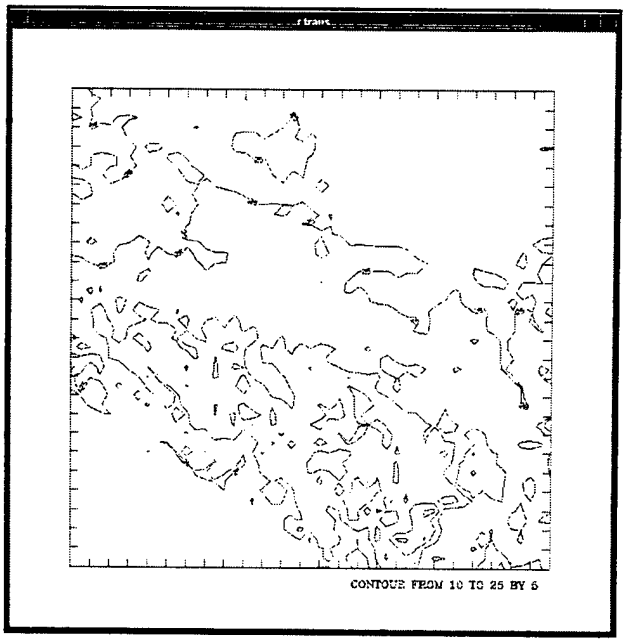

Figure 17. Same as figure 12, except T_0 = 6 h.

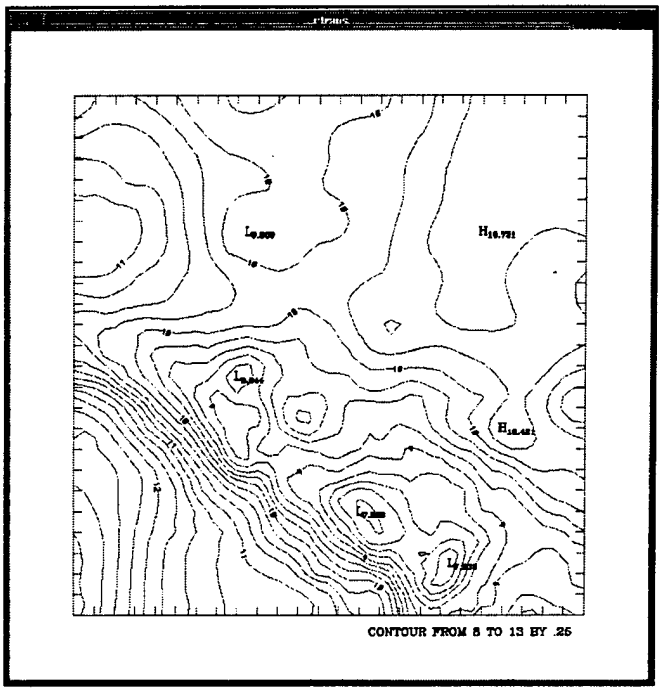

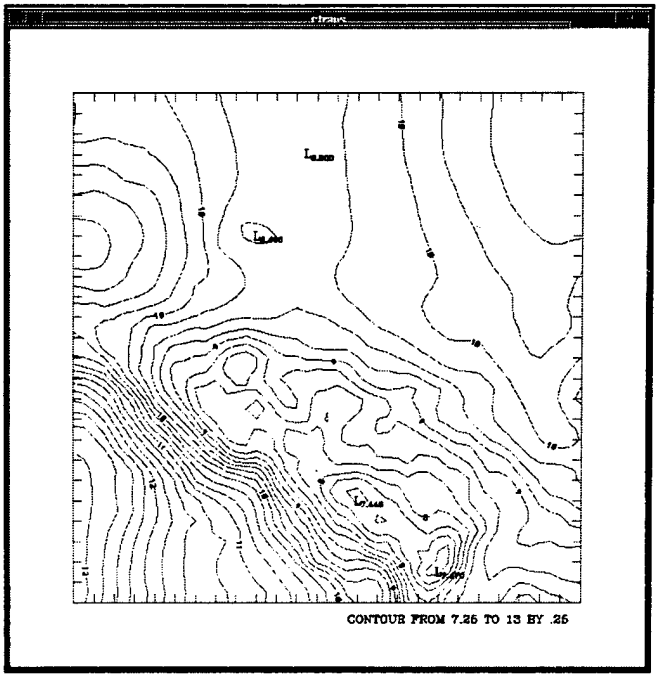

Figure 18. Same as figure 13, except for $T_0 = 3$ h.

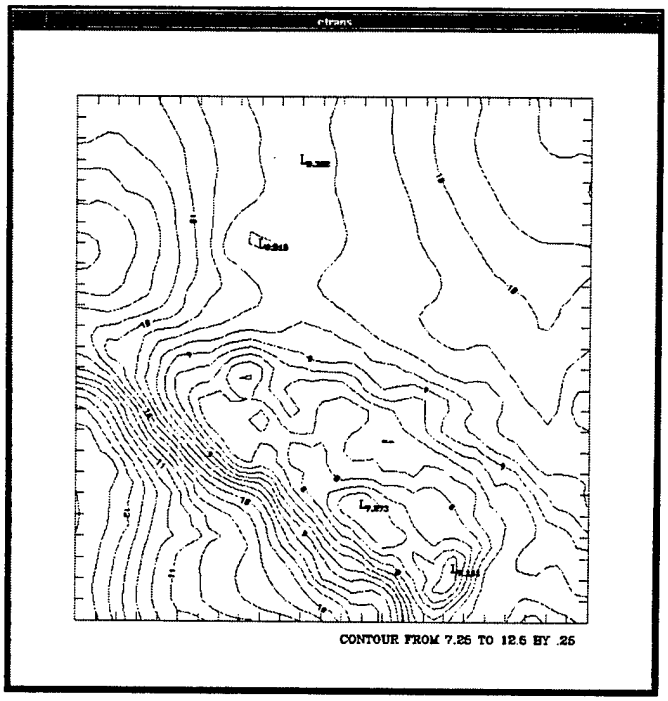

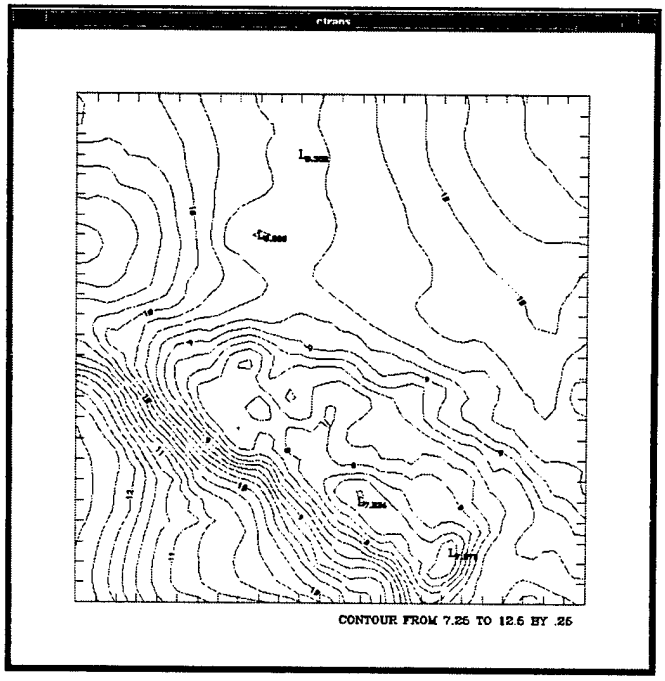

Figure 19. Same as figure 13, except for $T_0 = 6$ h.

6.4 Examples of Fog/Low Level Cloud and Non-Convective Precipitation

The BFM was applied to the Bosnia area for the 24-h period of 12 GMT, 19 December through 12 GMT, 20 December 1995. On 20 December 1995, the air traffic over the area was hampered by bad visibility and falling snow. The model simulated cloud formation over the area during the late evening of 19 December 1995, in addition to total cloud coverage over the entire model domain from 01 GMT to 12 GMT, 20 December 1995.

Figure 20 (top and bottom) show the cloud coverages at 23 GMT on 19 December 1995, and 00 GMT on 20 December 1995. The figures show the distribution of the weight of liquid water over a unit area (g /m^2). The darker the color, the denser the cloud. The figures may represent the cloud picture taken from far above. As can be seen, the area covered by cloud increased in the 1 h, and at 01 GMT on 20 December 1995, the entire area was covered by cloud.

Figure 21 shows the vertical profiles of total water content (g/kg), cloud water content (g/kg), and relative humidity (%), at the center point of the model domain. The top image represents 00 GMT, 20 December 1995, and the bottom represents 01 GMT, 20 December 1995. At 01 GMT, the entire area was covered by cloud. In 1 h, the modeled total water content increased significantly, and cloud water content profiles show significant increase in the lower atmosphere after 1 h. The relative humidity has also increased in 1 h, and a deep layer of the atmosphere has become saturated by 01 GMT. From the figures, it can be seen that a very small portion of total water is converted into cloud water.

Figure 22 shows the distribution of precipitation rate (mm/h) at 01 GMT on 20 December 1995. The precipitation rate was calculated by equation (170). The

figure shows the precipitation rate varied from 0.1 to 1.4 mm/h over the area. There was no precipitation over the model domain at 00 GMT.

It should be emphasized that fog/cloud and precipitation schemes in the model have yet to be thoroughly evaluated, and the results shown should be regarded as preliminary. Further study and development will be required.

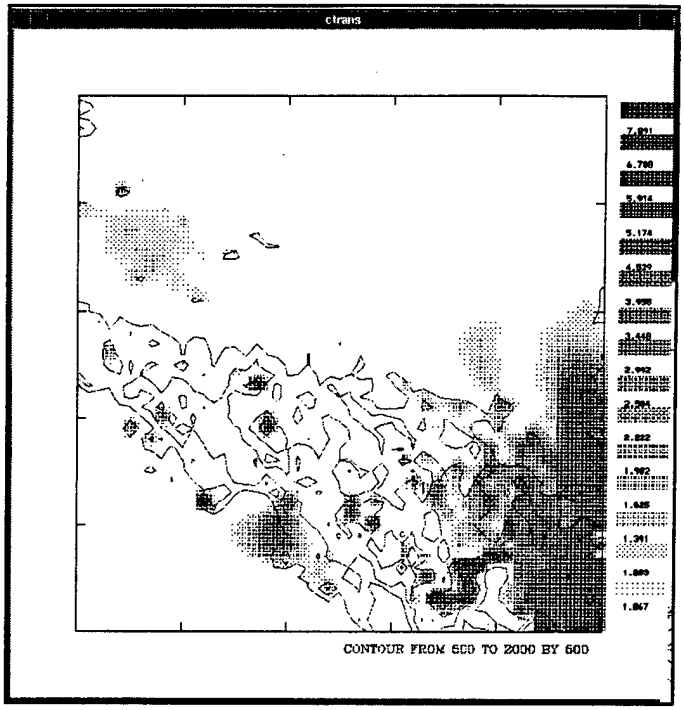

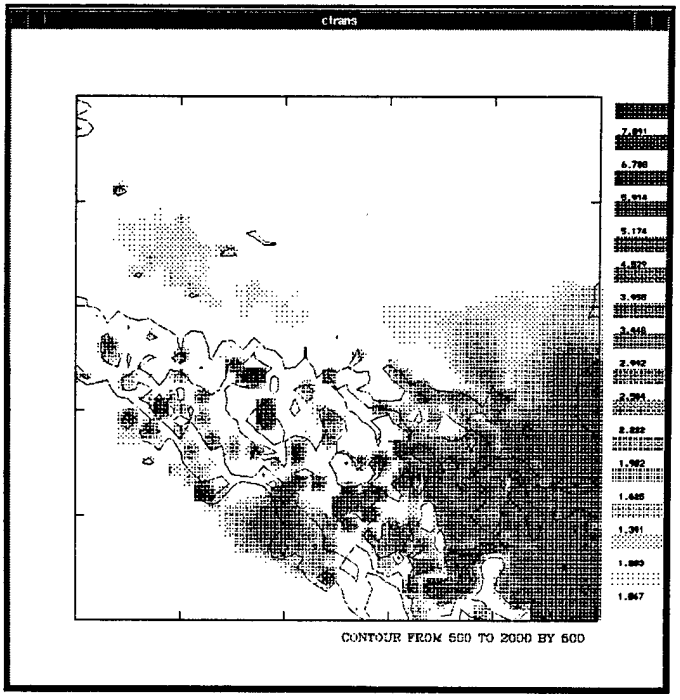

Figure 20. Cloud cover over Bosnia (top) at 23 GMT on 19 Dec 95, and at 00 GMT on 20 Dec 95 (bottom).

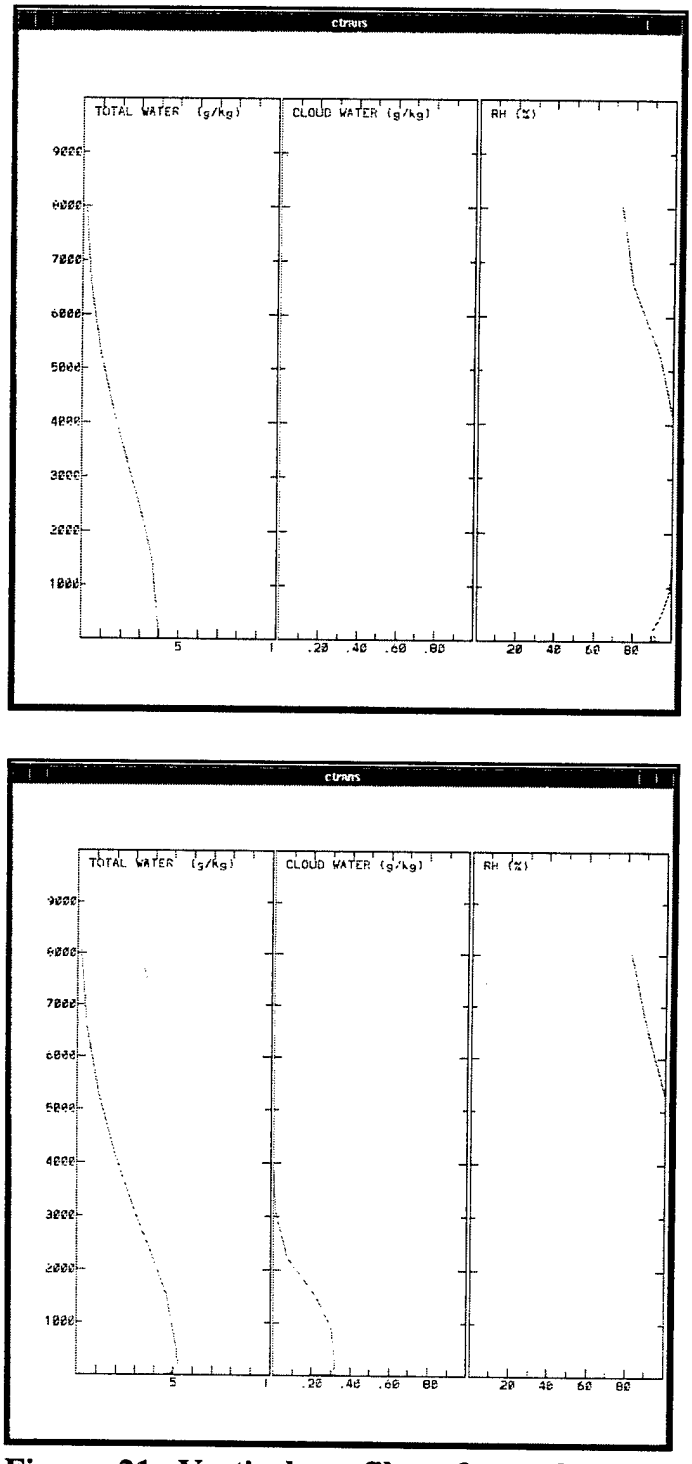

Figure 21. Vertical profiles of total water content (g/kg), cloud water content (g/kg), and relative humidity (%), at the center of model domain (top) at 00 GMT, and (bottom) at 01 GMT 20 Dec 95.

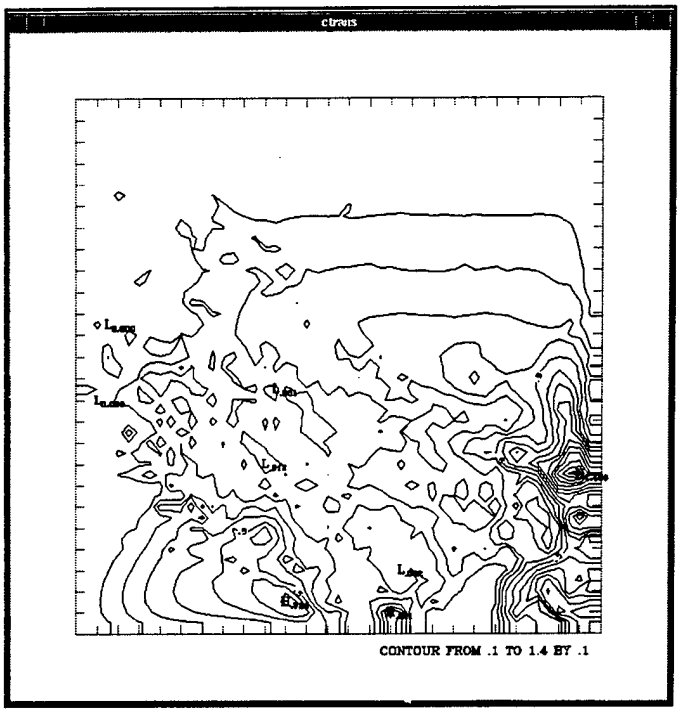

Figure 22. Precipitation rate (mm/h) distribution over Bosnia, at 01 GMT, 20 Dec 95. Maximum rate is 1.4 mm/h, and mimimum rate is .1 mm/h.

7. Conclusion

The forecasting period of the BFM has been extended to 24 h, and recently the forecast schemes for fog/cloud and as non-convective precipitation have been added. Other IMETS Block II software such as the Atmospheric Sounding Program (ASP) and the Integrated Weather Effects Decision Aids (IWEDA) utilize the BFM output file to calculate the values of their parameters. ASP generates products such as probability of thunderstorm occurrence, icing, visibility, turbulence, etc.

The terrain elevation data production scheme is executed from the BFM execution GUI when the BFM is applied to a new model area. For a typical model area of 500 x 500 km, meteorological data over an area extending to 1,600 x 1,600 km is used, so that typically four DTED CDROMs are required.

The three-dimensional objective analysis programs are also executed from the BFM execution GUI. Depending on the availability and quality of the input data (GSM, upper air sounding, and surface data), different combinations of input data are used to initialize the BFM. For all input data available, the BFM is initialized by the composited data fields from the GSM and upper air sounding data, plus surface sensor meteorological data. For a minimal requirement, the BFM can be initialized by a single sounding profile within the model domain and produce forecast field at to+ 6 h. During the 6-h forecast cycle, the model fields are nudged towards the initial fields (since no GSM lateral boundary conditions exist) but with an exponential damping in time identical to that used for surface nudging. The BFM execution GUI is capable of selecting the combination of input data.

The evaluation of the BFM forecasting capability is ongoing, and the results will be published in the future. Forecast capabilities of wind, temperature, and relative

humidity, as well as cloud coverage and non-convective precipitation amount distribution will be evaluated by comparing the model output and observed data.

The strengths of the BFM can be summarized as follows:

- The BFM is numerically stable and fast in calculation, and, as long as reasonable input data are used, the BFM produces numerically reasonable output. Currently, on the IMETS BLOCK II computer (SUN SPARC 20, 75 MHz, 256 MB RAM single processor), the BFM requires about 1.5 to 2 h of computing time for the 24-h forecast duration, using the model configuration of 51 x 51 x 16 grid points and 10 km horizontal grid spacing.

- Detailed atmospheric structures in the boundary layers can be seen. Sea and land breeze circulations, up-and-down valley winds, and diurnal variations of temperature due to surface heating/cooling are well simulated.

- GUI for the model execution and forecast displays are well designed and easy to use. Graphical displays of output include isoline contours and shaded color contour displays for scalar meteorological forecast parameters, and streamline and vector displays for wind.

- The BFM can be applied to any area of the world, as long as the input data for initialization and lateral boundary values are available.

The presently known limitations of the BFM are the following:

- Both hydrostatic and Boussinesq approximations are assumed. Extremely large changes in the large-scale temperature field advected into the BFM grid (via time-dependent boundary values resulting from the GSM) over 24 h could

possibly reduce the validity of the Boussinesq approximation, based on the BFM definition of the basic state for Θ_v such as, the basic state Θ_v that is the initially analyzed Θ_v field generated from the three-dimensional analysis).

- No cloud microphysics.

- No convective cloud parameterization, thus no ability to handle features generated by convective systems, such as meso-fronts (gust fronts), meso high/low, unless they are resolved by the initial fields.

- Rather crude specification of surface parameters, such as albedo, emissivity, soil moisture, snow, etc. These will be immediately addressed as real or near-real time data becomes readily available to the IMETS.

- Somewhat time-consuming to run at resolutions less than 5 km.

- A very coarse scale global model is currently used to provide lateral boundary conditions to the BFM.

Our future plan for further development includes:

- A BFM forecast capability that will be improved when the output of the regional scale forecast models, such as the U. S. Air Force's Relocatable Window Model (RWM) or the U.S. Navy Operational Regional Atmospheric Prediction System (NORAPS), is used instead of the GSM. We will start studying the utilization of regional scale model output to initialize the BFM and to provide its lateral boundary conditions.

- The inclusion of a cumulus/convective precipitation scheme will be made, by using currently available schemes, such as Sun and Haines and Kuo. [35], [36] Currently, we use 16 vertical layers with the model top 7000 m having the highest elevation in the model domain. To include a convective precipitation scheme, the number of vertical layers and the model depth will need to be increased.

- Evaluation studies of cloud/non-convective precipitation schemes by qualitatively comparing the model results with satellite photographs and NEXRAD estimated precipitation patterns, and quantitatively comparing precipitation records.

- Coding the three-dimensional analysis program of input data more efficiently, to shorten the overall forecast computational time.

References

1. Defense Mapping Agency, Fairfax, VA, "Digital Terrain Elevation Data (DTED) Level 1 Coverage," 1995.

2. Hoke, J.E., J.L. Haynes, and L.G. Renninger, "Map Projections and Grid Systems for Meteorological Applications," AFGWC/IN-79/003 (Rev), United States Air Force, Air Weather Service (MAC), Air Force Global Weather Central, Offutt AFB, NE 68113.

3. Barnes, S. L., NOAA Technical Memorandum ERL NSSL-62, U.S. Department of Commerce, National Oceanic and Atmospheric Administration, Environmental Research Laboratories, "Mesoscale Objective Map Analysis Using Weighted Time-Series Observations," 1973.

4. Yamada, T. and S. Bunker, "A Numerical Model Study of Nocturnal Drainage Flows with Strong Wind and Temperature Gradients," *Journal of Applied Meteorology*, 28, p. 545-554, 1989.

5. Yamada, T., "A Numerical Simulation of Nocturnal Drainage Flow," Journal of Meteorological Society of Japan, 59, p. 108 -122, 1981.

6. Yamada, T., "HOTMAC and RAPTAD, Three-Dimensional Atmospheric Transport and Diffusion Model, Program Operation Manual," Yamada Science & Art Corporation, p. 34, 1994.

7. Mellor, G. L. and T. Yamada, "A Hierachy of Turbulence-Closure Models for Planetary Boundary Layers," *Journal of Atmospheric Science*, 31, p. 1791-1806, 1974.

8. Sasamori, T., "The Radiative Cooling Calculation for Application to General Circulation Experiments," *Journal of Applied Meteorology*, 7, p. 721-729, 1968.

9. Yamada, T., "Simulations of Nocturnal Drainage Flows by a q^2l Turbulence Closure Model," *Journal of Atmospheric Sciences*, 40, p. 91-106, 1983.

10. Dyer, A. J. and B. B. Hicks, "Flux-Gradient Relationships in the Constant Flux Layer," *Quarterly Journal of Royal Meteorological Society*, 96, p. 715-721, 1970.

11. Panofsky, H. A., "Determination of Stress from Wind and Temperature Measurements," *Quarterly Journal of Royal Meteorological Society*, 89, p. 495-502,

12. Garratt, J. R. and B. B. Hicks, "Momentum, Heat, and Water Vapour Transfer to and from Natural and Artificial Surfaces," *Quarterly Journal of Royal Meteorological Society*, 99, p. 680-687, 1973.

13. Richtmyer, R. D. and K. W. Morton, "Difference Methods for Initial- Value Problems," Second Edition, Interscience Publishers, J. Wiley and Sons, New York, p. 405, 1963.

14. Kondrat'yev, K. Y., "Radiative Regime of Inclined Surface," WMO Technical Note No. 15, Secretariat of the World Meteorological Organization, Geneva, Switzerland, p. 82, 1977.

15. Paltridge, G. W. and C. M. R. Platt, "Radiative Processes in Meteorology and Climatology," Elesevier Scientific Publishing Company, New York, 1976.

16. Atwater, M. A. and P. S. Brown, Jr., "Numerical Calculation of the Latitudinal Variation of Solar Radiation for an Atmosphere of Varying Opacity," *Journal of Applied Meteorology*, 13, p. 289-297, 1974.

17. Kondat'yev, K. Y., "Radiation in the Atmosphere," Academic Press, New York, 1969.

18. Oliver, D. A., W. S. Lewellen, and G. G. Williamson, "The Interaction Between Turbulent and Radiative Transport in the Development of Fog and Low-Level Stratus," *Journal of Atmospheric Sciences*, 35, p. 301-316, 1978.

19. Fravalo, C., Y. Fouquart, and R. Rosset, "The Sensitivity of a Model of Low Stratiform Clouds to Radiatio," *Journal of Atmospheric Sciences*, 38, p. 1049-1062, 1981.

20. Hanson, H. P. and V. E. Derr, "Parameterization of Radiative Flux Profiles within Layer Clouds," *Journal of Applied Meterology*, 26, p. 1511-1521, 1987.

21. Wiscombe, W. J., R. M. Welch, and W. D. Hall, "The Effects of Very Large Drops on Cloud Absorption, Part I: Parcel Models," *Journal of Atmospheric Sciences*, 41, p. 1336-1355, 1984.

22. Cox, S. K., "Observation of Cloud Infrared Effective Emissivity," *Journal of Atmospheric Sciences*, 33, p. 287-289, 1976.

23. Yamada, T., "Assimilation of Battlefield Weather Data with a Forecast Model," Final Report to DAAL01-93-C-2009, U.S. Army Research Laboratory, unpublished report, 1994.

24. Stephens, G. L., S. Ackerman, and E. A. Smith, "A Shortwave Parameterization Revised to Improve Cloud Absorption," *Journal of Atmospheric Sciences*, 41, p. 687-690, 1984.

25. Betts, A. K., "Non-Precipitating Cumulus Convection and its Parameterization,"*Quarterly Journal of Royal Meteorological Society*, 99, p. 178-196, 1973.

26. Sommeria, G. and J. W. Deardorff, "Subgrid Scale Condensation in Cloud Models," *Journal of Atmospheric Sciences*, 34, p. 344-355, 1977.

27. Mellor, G. L., "The Gaussian Cloud Model Relation," *Journal of Atmospheric Sciences*, 34, p. 356-358, 1977.

28. Sundqvist, H., E. Berge, and J. E. Kristja'nsson, "Condensation and Cloud Parameterization Studies with a Mesoscale Numerical Weather Prediction Model," *Monthly Weather Review*, 117, p. 1641-1657, 1989.

29. Pielke, R. A., "Mesoscale Meteorological Modeling," Academic Press, New York, 1984.

30. Zack, J. W. et. al., "MASS Version 5.5 Reference Manual," MESO Inc. Report, March, 1993.

31. Yamada, T. and T. Henmi, "Four-Dimensional Assimilation of Large Scale Flow Field into Mesoscale Model," Proceedings of 93 Spring Meeting of Japan Meteorological Society, 1993.

32. Henmi, T., M. E. Lee, and T. J. Smith, "Evaluation of the Battlescale Forecast Model (BFM)," Proceedings of the 1994 Battlefield Atmospherics Conference,

Battlefield Environment Directorate, U.S. Army Research Laboratory, White Sands Missile Range, NM, 1995.

33. Knapp, D. and R. Dumais, "Statistical Evaluation of the BFM," to be published as a U.S. Army Technical Report, 1996.

34. U.S. Air Force Global Weather Central, "T - TWOS, Global Spectral Model Forecast Package, User's Manual," T - TWOS No. 13, 1992.

35. Sun, W. Y. and P. A. Haines, "Semi-Prognostic Tests of a New Cumulus Parameterization Scheme for Mesoscale Modeling," *Tellus*, 48A, p. 272-289, 1996.

36. Kuo, H. L., "On Formation and Intensification of Tropical Cyclones Through Latent Heat Release by Cumulus Convection," *Journal of Atmospheric Sciences*, 22, p. 40-63, 1965.

Acronyms and Abbreviations

AFGWC	Air Force Global Weather Center
AGL	above ground level
ARL	Army Research Laboratory
ASL	above sea level
ASP	Atmospheric Sounding Program
ATRAD	atmospheric radiation
AWDS	Automated Weather Distribution System
BED	Battlefield Environment Directorate
BFM	Battlescale Forecast Model
CDROM	Compact Disk Read Only Memory
DMA	Defense Mapping Agency
DTED	Digital Terrain Elevation Data
DTED1	Level 1 Digital Terrain Elevation Data
GMT	Greenwich Meridian Time
GSM	Global Spectral Model
GUI	Graphical User Interface
HOTMAC	Higher Order Turbulence Model of Atmospheric Circulation
IMETS	Integrated Meteorological System
IWEDA	Integrated Weather Effects Decision Aids
MSL	mean sea level
NORAPS	Navy Operational Regional Atmospheric Prediction System
RWM	Relocatable Window Model
WSMR	White Sands Missile Range

Appendix

List of Symbols

A	tridiagonal matrix
	expression by eq. (88)
	coefficient of a linear relationship y=A + Bx
A_b	absorption of short-wave radiation in cloud
a	parameter defined by eq. (119)
	parameter defined by eq. (150)
B	column vector
	Bowen ratio (= H_s/LE)
	empirical constant (= 16.6)
	expression by eq. (89)
	coefficient of a linear relationship y = A + Bx
B_B	parameter defined by eq. (134)
B_c	parameter defined by eq. (133)
b	parameter defined by eq. (120)
	parameter defined by eq. (151)
C	expression by eq. (90)
C_n	nudging coefficient
$C_{n,\,new}$	nudging parameter for surface data
C_p	specific heat of air at constant pressure
C_0	parameter, $1/C_0$ is a characteristic time for conversion of cloud droplets to precipitation
C_{0F}	parameter defined by eq. (171)
C_1	empirical parameter (= 0.1)
c	constant (= 0.01)
	parameter defined by eq. (121)

D	parameter defined by eq. (127)
d	mean distance
E_l	expression by eq. (83)
e	water vapor pressure
e_s	saturation water vapor pressure
F_B	parameter defined by eq. (123)
F_{BF}	temperature function defined by eq. (170)
$F_B\downarrow$	downward solar flux at the top of cloud
F_c	parameter defined by eq. (118)
F_l	expression by eq. (8)
F_1	empirical constant (= 1.8)
	right-hand side of eq. (35)
F_2	empirical constant (= 1.33)
	right-hand side of eq. (36)
F_3	right-hand side of eq. (46)
F_4	right-hand side of eq. (44)
F_∞	parameter defined by eq. (169)
f	Coriolis parameter
G	ground heat flux
	solar radiation reaching the surface
	probability density function for cloud formation
G(z)	infrared flux profile in the layered cloud
$G_B\downarrow$	downward long-wave flux at the cloud top
$G_c\uparrow$	upward long-wave flux at the cloud base
G_L	parameter defined by eq. (125)

G_U	parameter defined by eq. (126)
G_0	parameter defined by eq. (129)
G_1	parameter defined by eq. (130)
g	acceleration of gravity
H	material surface top of the model in z coordinate
$\overline{H}$	material surface top of z* coordinate
H(x)	Heaviside function
H_s	sensible heat flux
i_{max}	maximum number of grid points in x direction
J_d	Julian date
j_{max}	maximum number of grid points in y direction
K_s	heat conductivity of soil
K_x	horizontal eddy diffusivity in x direction ($=2c(\Delta x)(\Delta y)\lvert \partial U/\partial x \rvert$)
K_{xy}	horizontal eddy diffusivity in xy direction ($=c(\Delta x)(\Delta y)\{\lvert \partial U/\partial x \rvert + \lvert \partial V/\partial y \rvert \}$)
K_y	horizontal eddy diffusivity in y direction ($=2c(\Delta x)(\Delta y)\lvert \partial V/\partial y \rvert$)
k	empirical parameter to determine the shape of weighting function von Karman constant
L	Obukhov length
LE	latent heat flux
L_v	latent heat of condensation
l	turbulence length scale
m	function defined by eq. (78)
n	time-step
P	pressure

	rate of release of precipitation
P_{gr}	surface pressure
P_r	turbulence Prandtl number
P_1	pressure at height Φ_1
P_2	pressure at height Φ_2
$Q_{c,cr}$	threshold value for cloud water to produce precipitation
$Q_{(c,\,cr)F}$	parameter defined by eq. (172)
Q_1	parameter defined by eq. (160)
Q_l	mixing ratio of liquid water
Q_s	saturation mixing ratio
Q_*	scale of moisture
q	water vapor mixing ratio
$q^2/2$	turbulence kinetic energy of unit mass of the air ($q^2=u^2+v^2+w^2$)
R	parameter defined by eq. (115)
	fraction of cloud coverage
R_d	gas constant of the dry air
R_e	reflection of short-wave in cloud
R_N	long-wave radiation flux
R_E	radius of the earth
Ri_f	flux Richardson number
Ri_g	gradient Richardson number
Ri_c	critical flux Richardson number
$R_{L\downarrow}$	incoming long-wave radiation
$R_{L\uparrow}$	outgoing long-wave radiation
R_s	incoming direct solar radiation

R_w	gas constant for water vapor
R_0	near-surface direct solar radiation flux
R_{0s}	incoming radiation at the top of the atmosphere
$R_0\downarrow$	long-wave incoming radiation to horizontal surface
$r_{ij,N}$	normalized distance between a grid point (i, j) and Nth GSM point.
S_c	turbulence Schmidt number
S_l	empirical constant (= 0.2)
S_M	function of flux Richardson number, defined by eq. (49)
S_q	empirical constant (= 0.2)
T	temperature
T_B	absolute temperature at cloud top
T_c	absolute temperature at cloud base
T_d	dew point temperature
T_G	ground surface temperature
T_g	soil surface temperature
T_l	liquid water temperature
T_r	transmission of short-wave radiation in cloud
T_s	soil temperature
T_v	virtual temperature
T_1	temperature at height Φ_1
T_2	temperature at height Φ_2
T_*	scale of temperature
t	dimensionless longitudinal distance defined by eq. (3)
$t_{c,t}$	clock time
t_{eq}	equation of time defined by eq. (94)

t_s	true solar time
U	east-west component of horizontal wind vector
u	dimensionless latitudinal distance defined by eq. (4)
	parameter defined by eq. (111)
U_g	east-west component of geostrophic wind vector
U_t	east-west component of target wind vector
U'	x component of horizontal wind vector in the GSM
u_*	friction velocity
V	north-south component of horizontal wind vector
V_g	north-south component of geostrophic wind
V_t	north-south component of target wind vector
V'	y component of horizontal wind vector in the GSM
W	vertical component of wind vector in the Cartesian coordinate
	total cloud liquid water content
W'	vertical component of wind vector in z* coordinate
Z	DTED elevation data
	average height
z	Cartesian vertical coordinate
z_B	cloud top height
z_c	cloud base height
z*	vertical coordinate used in the BFM
z_g	ground elevation
z_{gmax2}	maximum value of the terrain elevation in the data collection
	1600 x 1600 km domain

z_{gmax}	maximum value of the terrain elevation in the BFM 500 x 500 km domain
z_{st}	Cartesian height above sea level of z*
z_0	roughness length for wind
z_{0t}	roughness length for temperature
z_{0v}	roughness length for water vapor
zcrit	model level nearest to 1500 m AGL used to compute geostrophic winds
α	function of flux Richardson number, defined by eq. (51)
	angle of inclination to the sloped surface to the horizontal plane
$\alpha\uparrow$	coefficient (= 0.13)
$\alpha\downarrow$	coefficient (= 0.158)
β	backscattered fraction of monodirectional incident radiation
γ	empirical weight reduction factor
Δ	dew point depression
	unit grid space
Δ_n	defined as $\Psi_n - \Psi_n'$
Δt_{long}	longitudinal correction to time
δ	declination of the sun
ϵ	emissivity of the surface
ζ	non-dimensional height (= z/L)
κ	ratio of R/C_p
Θ	potential temperature
Θ_l	liquid potential temperature
Θ_v	virtual potential temperature

θ_v	fluctuation of virtual potential temperature
θ_0	angle in rads related to the Julian date defined by eq. (87)
λ	longitude of the GSM grid point
	smoothing factor (0.25 or 0.5)
	wave length
λ_N	parameter defined by eq. (128)
λ_L	parameter defined by eq. (135)
λ_U	parameter defined by eq. (136)
λ'	function of λ defined by eq. (7)
μ_0	zenith angle
Π	modified pressure
ρ	air density
σ	Stefan-Boltzman constant
$\sigma_{\theta l}$	parameter defined by eq. (145)
σ_{qw}	parameter defined by eq. (146)
σ_s	parameter defined by eq. (161)
τ_N	optical thickness of cloud
τ_{eff}	variable defined by eq. (114)
Φ	geopotential height
	latitude
ϕ_m	non-dimensional wind profile
ϕ_h	non-dimensional temperature profile
ϕ_v	non-dimensional moisture profile
Ψ	arbitrary variable
φ	arbitrary variable

Ψ_h	empirical function to correct the profile of temperature
Ψ_m	empirical function to correct the profile of wind
Ψ_n	azimuth of the projection of the normal to the surface on horizontal plane
Ψ_v	empirical function to correct the profile of moisture
Ψ'	parameter defined by eq. (16)
Ω	solar hour angle
ϖ_0	single scattering albedo

Distribution

	Copies
NASA MARSHAL SPACE FLT CTR ATMOSPHERIC SCIENCES DIV E501 ATTN DR FICHTL HUNTSVILLE AL 35802	1
NASA SPACE FLT CTR ATMOSPHERIC SCIENCES DIV CODE ED 41 1 HUNTSVILLE AL 35812	1
ARMY STRAT DEFNS CMND CSSD SL L ATTN DR LILLY PO BOX 1500 HUNTSVILLE AL 35807-3801	1
ARMY MISSILE CMND AMSMI RD AC AD ATTN DR PETERSON REDSTONE ARSENAL AL 35898-5242	1
ARMY MISSILE CMND AMSMI RD AS SS ATTN MR H F ANDERSON REDSTONE ARSENAL AL 35898-5253	1
ARMY MISSILE CMND AMSMI RD AS SS ATTN MR B WILLIAMS REDSTONE ARSENAL AL 35898-5253	1
ARMY MISSILE CMND AMSMI RD DE SE ATTN MR GORDON LILL JR REDSTONE ARSENAL AL 35898-5245	1
ARMY MISSILE CMND REDSTONE SCI INFO CTR AMSMI RD CS R DOC REDSTONE ARSENAL AL 35898-5241	1
ARMY MISSILE CMND AMSMI REDSTONE ARSENAL AL 35898-5253	1

CMD (420000D(C0245)) 1
ATTN DR A SHLANTA
NAVAIRWARCENWPNDIV
1 ADMIN CIR
CHINA LAKE CA 93555-6001

PACIFIC MISSILE TEST CTR 1
GEOPHYSICS DIV
ATTN CODE 3250
POINT MUGU CA 93042-5000

NAVAL OCEAN SYST CTR 1
CODE 54
ATTN DR RICHTER
SAN DIEGO CA 52152-5000

METEOROLOGIST IN CHARGE 1
KWAJALEIN MISSILE RANGE
PO BOX 67
APO SAN FRANCISCO CA 96555

DEPT OF COMMERCE CTR 1
MOUNTAIN ADMINISTRATION
SPPRT CTR LIBRARY R 51
325 S BROADWAY
BOULDER CO 80303

DR HANS J LIEBE 1
NTIA ITS S 3
325 S BROADWAY
BOULDER CO 80303

NCAR LIBRARY SERIALS 1
NATL CTR FOR ATMOS RSCH
PO BOX 3000
BOULDER CO 80307-3000

DEPT OF COMMERCE CTR 1
325 S BROADWAY
BOULDER CO 80303

DAMI POI 1
WASHINGTON DC 20310-1067

MIL ASST FOR ENV SCI OFC 1
OF THE UNDERSEC OF DEFNS
FOR RSCH & ENGR R&AT E LS
PENTAGON ROOM 3D129
WASHINGTON DC 20301-3080

DEAN RMD
ATTN DR GOMEZ
WASHINGTON DC 20314 1

ARMY INFANTRY
ATSH CD CS OR
ATTN DR E DUTOIT
FT BENNING GA 30905-5090 1

AIR WEATHER SERVICE
TECH LIBRARY FL4414 3
SCOTT AFB IL 62225-5458 1

USAFETAC DNE
ATTN MR GLAUBER
SCOTT AFB IL 62225-5008 1

HQ AFWA/DNX
106 PEACEKEEPER DR STE 2N3
OFFUTT AFB NE 68113-4039 1

PHILLIPS LABORATORY
PL LYP
ATTN MR CHISHOLM
HANSCOM AFB MA 01731-5000 1

ATMOSPHERIC SCI DIV
GEOPHYISCS DIRCTRT
PHILLIPS LABORATORY
HANSCOM AFB MA 01731-5000 1

PHILLIPS LABORATORY
PL LYP 3
HANSCOM AFB MA 01731-5000 1

ARMY MATERIEL SYST
ANALYSIS ACTIVITY
AMXSY
ATTN MR H COHEN
APG MD 21005-5071 1

ARMY MATERIEL SYST
ANALYSIS ACTIVITY
AMXSY AT
ATTN MR CAMPBELL
APG MD 21005-5071 1

ARMY MATERIEL SYST
ANALYSIS ACTIVITY
AMXSY CR
ATTN MR MARCHET
APG MD 21005-5071 1

ARL CHEMICAL BIOLOGY
NUC EFFECTS DIV
AMSRL SL CO
APG MD 21010-5423 1

ARMY MATERIEL SYST
ANALYSIS ACTIVITY
AMSXY
APG MD 21005-5071 1

ARMY MATERIEL SYST
ANALYSIS ACTIVITY
AMXSY CS
ATTN MR BRADLEY
APG MD 21005-5071 1

ARMY RESEARCH LABORATORY
AMSRL D
2800 POWDER MILL ROAD
ADELPHI MD 20783-1145 1

ARMY RESEARCH LABORATORY
AMSRL OP SD TP
TECHNICAL PUBLISHING
2800 POWDER MILL ROAD
ADELPHI MD 20783-1145 1

ARMY RESEARCH LABORATORY
AMSRL OP CI SD TL
2800 POWDER MILL ROAD
ADELPHI MD 20783-1145 1

ARMY RESEARCH LABORATORY
AMSRL SS SH
ATTN DR SZTANKAY
2800 POWDER MILL ROAD
ADELPHI MD 20783-1145 1

ARMY RESEARCH LABORATORY
AMSRL
2800 POWDER MILL ROAD
ADLEPHI MD 20783-1145 1

NATIONAL SECURITY AGCY W21
ATTN DR LONGBOTHUM
9800 SAVAGE ROAD
FT GEORGE G MEADE MD 20755-6000 1

ARMY RSRC OFC
ATTN AMXRO GS (DR BACH)
PO BOX 12211
RTP NC 27009 1

DR JERRY DAVIS 1
NCSU
PO BOX 8208
RALEIGH NC 27650-8208

US ARMY CECRL 1
CECRL GP
ATTN DR DETSCH
HANOVER NH 03755-1290

ARMY ARDEC 1
SMCAR IMI I BLDG 59
DOVER NJ 07806-5000

ARMY COMMUNICATIONS 1
ELECTR CTR FOR EW RSTA
AMSEL EW D
FT MONMOUTH NJ 07703-5303

ARMY COMMUNICATIONS 1
ELECTR CTR FOR EW RSTA
AMSEL EW MD
FT MONMOUTH NJ 07703-5303

ARMY DUGWAY PROVING GRD 1
STEDP MT DA L 3
DUGWAY UT 84022-5000

ARMY DUGWAY PROVING GRD 1
STEDP MT M
ATTN MR BOWERS
DUGWAY UT 84022-5000

DEPT OF THE AIR FORCE 1
OL A 2D WEATHER SQUAD MAC
HOLLOMAN AFB NM 88330-5000

PL WE 1
KIRTLAND AFB NM 87118-6008

USAF ROME LAB TECH 1
CORRIDOR W STE 262 RL SUL
26 ELECTR PKWY BLD 106
GRIFFISS AFB NY 13441-4514

AFMC DOW 1
WRIGHT PATTERSON AFB OH 45433-5000

ARMY FIELD ARTILLERY SCHOOL 1
ATSF TSM TA
FT SILL OK 73503-5600

ARMY FOREIGN SCI TECH CTR
CM
220 7TH STREET NE
CHARLOTTESVILLE VA 22448-5000 1

NAVAL SURFACE WEAPONS CTR
CODE G63
DAHLGREN VA 22448-5000 1

ARMY OEC
CSTE EFS
PARK CENTER IV
4501 FORD AVE
ALEXANDRIA VA 22302-1458 1

ARMY CORPS OF ENGRS
ENGR TOPOGRAPHICS LAB
ETL GS LB
FT BELVOIR VA 22060 1

ARMY TOPO ENGR CTR
CETEC ZC 1
FT BELVOIR VA 22060-5546 1

SCI AND TECHNOLOGY
101 RESEARCH DRIVE
HAMPTON VA 23666-1340 1

ARMY NUCLEAR CML AGCY
MONA ZB BLDG 2073
SPRINGFIELD VA 22150-3198 1

USATRADOC
ATCD FA
FT MONROE VA 23651-5170 1

ARMY TRADOC ANALYSIS CTR
ATRC WSS R
WSMR NM 88002-5502 1

ARMY RESEARCH LABORATORY
AMSRL IS S
BATTLEFIELD ENVIR DIR
WSMR NM 88002-5501 1

ARMY RESEARCH LABORATORY
AMSRL IS E
BATTLEFIELD ENVIR DIR
WSMR NM 88002-5501 1

ARMY RESEARCH LABORATORY AMSRL IS W BATTLEFIELD ENVIR DIR WSMR NM 88002-5501	1
DTIC 8725 JOHN J KINGMAN RD STE 0944 FT BELVOIR VA 22060-6218	1
ARMY MISSILE CMND AMSMI REDSTONE ARSENAL AL 35898-5243	1
ARMY DUGWAY PROVING GRD STEDP3 DUGWAY UT 84022-5000	1
USTRADOC ATCD FA FT MONROE VA 23651-5170	1
WSMR TECH LIBRARY BR STEWS IM IT WSMR NM 88001	1
US MILITARY ACADEMY MATHEMATICAL SCI CTR EXCELLENCE DEPT OF MATHEMATICAL SCIENCES ATTN MDN A (MAJ DON ENGEN) THAYER HALL WEST POINT NY 10996-1786	1
ARMY RESEARCH LABORATORY INFORMATION SCIENCE & TECHNOLOGY BATTLEFIELD ENVIRONMENT DIVISION AMSRL IS EW ATTN DR TEIZI HENMI WSMR NM 88002 5504	10
ARMY RESEARCH LABORATORY INFORMATION SCIENCE & TECHNOLOGY BATTLEFIELD ENVIRONMENT DIVISION AMSRL IS EW ATTN MR ROBERT DUMAIS WSMR NM 88002 5504	5

INFORMATION SCIENCE & TECHNOLOGY BATTLEFIELD ENVIRONMENT DIVISION AMSRL IS EW ATTN MR JAMES HARRIS WSMR NM 88002 5504	1
ARMY RESEARCH LABORATORY INFORMATION SCIENCE & TECHNOLOGY BATTLEFIELD ENVIRONMENT DIVISION AMSRL IS EW ATTN DR DOUGLAS BROWN WSMR NM 88002 5504	1
Record Copy	1
TOTAL	88